Title: Magnetic Refrigeration Technology for High Efficiency Air Conditioning (public version)

Report Type: Final

Reporting Period: October 1, 2003 – September 29, 2006

Principal Authors: A. Boeder, Astronautics Corporation of America
C. Zimm, Astronautics Corporation of America

Report Date: December 22, 2006

Award Number: DE-FC26-03NT41948

Name and address of submitting organization:
Astronautics Corporation of America
4115 N. Teutonia Avenue
Milwaukee, WI 53209

I Abstract

Magnetic refrigeration was investigated as an efficient, environmentally friendly, flexible alternative to conventional residential vapor compression central air conditioning systems. Finite element analysis (FEA) models of advanced geometry active magnetic regenerator (AMR) beds were developed to minimize bed size and thus magnet mass by optimizing geometry for fluid flow and heat transfer and other losses. Conventional and magnetocaloric material (MCM) regenerator fabrication and assembly techniques were developed and advanced geometry passive regenerators were built and tested. A subscale engineering prototype (SEP) magnetic air conditioner was designed, constructed and tested. A model of the AMR cycle, combined with knowledge from passive regenerator experiments and FEA results, was used to design the regenerator beds. A 1.5 Tesla permanent magnet assembly was designed using FEA and the bed structure and plenum design was extensively optimized using FEA. The SEP is a flexible magnetic refrigeration platform, with individually instrumented beds and high flow rate and high frequency capability, although the current advanced regenerator geometry beds do not meet performance expectations, probably due to manufacturing and assembly tolerances. A model of the AMR cycle was used to optimize the design of a 3 ton capacity magnetic air conditioner, and the system design was iterated to minimize external parasitic losses such as heat exchanger pressure drop and fan power. The manufacturing cost for the entire air conditioning system was estimated, and while the estimated SEER efficiency is high, the magnetic air conditioning system is not cost competitive as currently configured. The 3 ton study results indicate that there are other applications where magnetic refrigeration is anticipated to have cost advantages over conventional systems, especially applications where magnetic refrigeration, through the use of its aqueous heat transfer fluid, could eliminate intermediate heat exchangers or oil distribution issues found in traditional vapor compression systems.

II Table of Contents

III List of Graphical Materials

Figures

Tables

IV Executive Summary

Magnetic refrigeration was investigated as an efficient, environmentally friendly, flexible alternative to conventional residential vapor compression central air conditioning systems.

An existing rotating bed magnetic refrigerator was used to test first order magnetocaloric materials (MCM) as well as a layered bed containing MCMs with two different Curie temperatures. These results were compared with results for single layer, second order MCMs. Materials were tested over a range of flow rates, frequencies, and temperatures.

Tests with one first order MCM, $Gd_5(Si_{2.09}Ge_{1.91})_4$, showed that this particular material suffers from hysteresis or other frequency dependent effects, with performance decreasing with increasing operating frequency. Another first order MCM, LaFeSiH, tested under a parallel NIST ATP program, did not exhibit the same degree of hysteresis, and appears to be very promising magnetocaloric refrigerant.

Testing a bed layered with pure Gd and a Gd-Er alloy clearly demonstrated the importance of layering. The layered bed performed better than beds containing either of the constituent MCMs alone, producing more cooling power and a larger temperature span. Layering is critical to produce a useful temperature span with first order MCM's. First order MCMs and layering have the potential to greatly improve the performance of magnetic refrigeration.

Multiple advanced passive regenerators were fabricated and tested with conventional materials. These beds served as proxies for active magnetic regenerators because the losses that occur during the regeneration portion of the active magnetic regenerator cycle also occur in passive regenerators. The tests compared regenerators by measuring ineffectiveness over a range of flow rates and cycle frequencies.

Various advanced regenerator beds were designed, using finite element analysis and regenerator cycle models to optimize the geometry. Beds were then fabricated and tested as passive regenerators. Higher than expected losses were observed, likely caused by manufacturing and assembly tolerances. The performance was lower than that of baseline tests conducted with spherical particle, irregular particle, and packed screen regenerator beds. A bed with a modified design improved performance, but the results did not meet expectations, indicating the geometry was still sensitive to tolerances. Fabrication tests with Gd indicated greater challenges in holding tolerances.

The next passive regenerator design used another method to order to control the critical flow path size instead of metal features. Performance of this regenerator did not meet expectations. We suspect that geometry variation caused flow maldistribution, resulting in reduced heat transfer.

Measuring the properties of Gd and Gd alloys verified that the magnetocaloric properties of Gd-Er alloys changed smoothly with Er content, and the properties different shapes are essentially the same as that of bulk material and of spherical particles.

A rotating permanent magnet-based subscale engineering prototype (SEP) magnetic refrigerator was constructed. The SEP produced good cooling power, coming very close to model predictions for the zero-span case, but the temperature span is smaller than expected. We suspect the reduced performance originates from flow maldistribution within the Gd beds, likely caused by geometry variation due to material inconsistencies and assembly tolerances.

The SEP is a flexible test platform, with individual, fixed beds that can be individually instrumented. The SEP operates at high flow rate and frequency, allowing us to push the limits of future high performance beds. The high speed data acquisition system is flexible and expandable for future experiments, and a unique torque meter arrangement allows measurement of the magnet drive torque and/or the valve drive torque.

TIAX LLC developed the projected cost for 3 ton magnetic air conditioning (MAC) systems. The MAC model included parasitic losses internal to the regenerator beds, along with losses associated with fluid pumping, heat leaks and fan power. The MAC model also used future advanced regenerators and improved materials. The magnet cost was based on a detailed Astronautics design. TIAX went through multiple optimization iterations using Heatcraft code to minimize the heat exchanger cost.

The limiting factor during modeling the high efficiency MAC was the baseline EER rather than the resulting SEER, because a MAC tends to operate efficiently at part load.

Comparing the direct manufacturing cost of a high efficiency MAC to a conventional high efficiency vapor compression (VC) system, the MAC is 28% more efficient and 37% more costly. The cost gap closes with higher efficiency. Magnets dominate the MAC cost. Improving the MCM, with a material with higher magnetocaloric effect than LaFeSiH, would further reduce the cost. TIAX also produced a cost stack for a lower cost, lower efficiency version of the MAC, but the cost comparison was less favorable.

While this analysis showed that magnetic refrigeration is not currently projected to be less expensive than conventional technology in the residential 3 ton capacity ducted air conditioning application, there are other applications where MAC is anticipated to have cost advantages over conventional systems, especially applications where magnetic refrigeration, through the use of its aqueous heat transfer fluid, could eliminate intermediate heat exchangers or oil distribution issues found in tradition vapor compression systems.. Examples include ductless split systems, specifically larger capacity (8-20 tons) variable refrigerant flow systems, and water cooled chillers.

1 Experimental

1.1 Introduction: How the AMR works

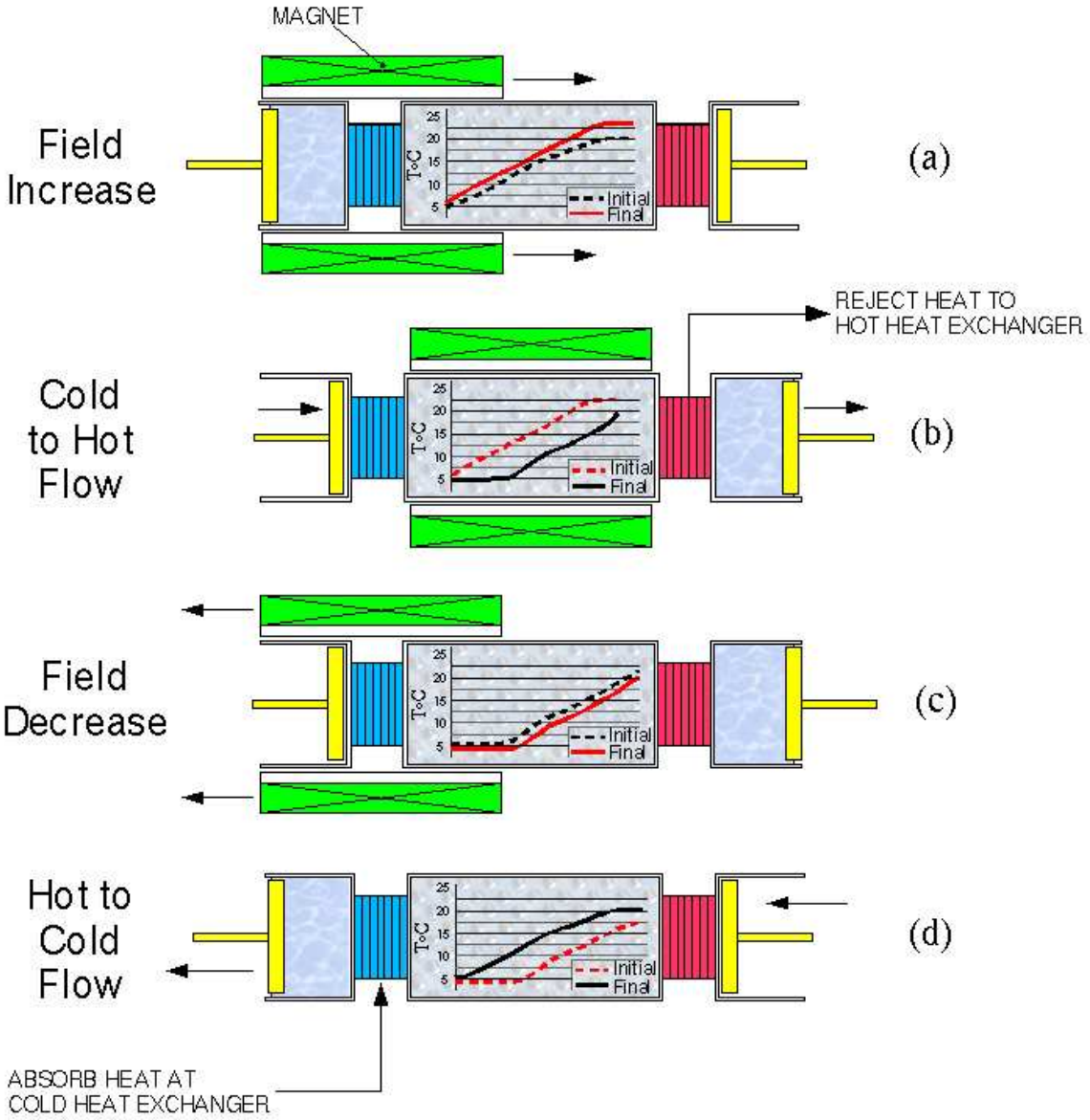

Figure 1.1: The Active Magnetic Regenerative cycle.

A regenerative or recuperative refrigeration cycle is required for operation over a temperature span larger than the magnetocaloric material's ΔT_{ad}. Astronautics successfully demonstrated before the start of this program that the Active Magnetic Regenerator (AMR) cycle can achieve the large temperature span required for many refrigeration applications. In this cycle a magnetocaloric material (MCM) matrix, suffused with a fluid, is alternately magnetized and demagnetized. The MCM matrix, or bed, generates refrigeration that regenerates the bed itself, using the thermal linkage of the fluid. The fluid also carries heat to and from external heat exchangers (HEXs).

The AMR cycle is operated as shown in Fig 1.1 for a steady state condition. An example is shown where the hot HEX is at 21 C and the cold HEX is at 5 C. In Fig 1.1a, the initial temperature profile is for the bed in its demagnetized state in zero magnetic field (dashed line). When a magnetic field is applied to the refrigerant, each particle in the bed warms because of the magnetocaloric effect to form the final magnetized bed temperature profile (solid line). The amount each particle warms is equal to the adiabatic temperature change upon magnetization at the initial temperature of the particle, reduced by the effect of the heat capacity of the fluid in the pores between the particles. Next, the cold fluid flows through the bed from the cold end to the hot end (Fig. 1.1b). The bed is cooled by the fluid, lowering the temperature profile across the bed, and the fluid in turn is warmed by the bed, emerging at a temperature close to the temperature of the bed at the warm end. This temperature is higher than 21 C, so heat is removed from the fluid at the hot heat sink as the fluid flows through the hot HEX. After the fluid flow is stopped, the magnetic field is removed, cooling the bed by the magnetocaloric effect (Fig. 1.1c). The refrigeration cycle is completed by forcing the fluid to flow from the hot to the cold end of the bed (Fig. 1.1d). The fluid is cooled by the bed, emerging at a temperature below 5 C and removes heat from the cold sink as the fluid passes through the cold HEX. The heat flow from cold to hot in this cycle is driven by the net mechanical work input needed to move the magnet with respect to the magnetocaloric bed. The higher magnetization of the cold matrix results in a greater force to remove the magnet from the matrix than to initially cover the warmer, lower magnetization, matrix by the magnet.

1.2 Rotary bed magnetic refrigerator experiments.

1.2.1 Description of RBMR.

The Rotating Bed Magnetic Refrigerator (RBMR) is a near room temperature magnetic refrigeration device built by Astronautics in 2001, shown in Figure 1.2. The RBMR utilizes a nominal 1.5 Tesla stationary permanent magnet and a rotating wheel that contains six active magnetic regenerator (AMR) beds. Rotary disk valves located coaxially with the bed wheel control heat transfer fluid flow to the beds.

An electric heater provides a measurable heat load to fluid flowing on the cold side, while a brazed plate heat exchanger connected to a temperature controlled circulating bath controls the heat rejection temperature. The wheel drive motor and the pump both have variable speed drives to control the cycle frequency and fluid flow rate, respectively. For this project, installing a new variable speed DC gear motor enabled exploring rotational frequencies up to 5 Hz.

Instrumentation includes pressure sensors, a flow meter, hot and cold inlet and outlet temperature sensors, rotation speed sensor, and drive motor, pump, and heater voltage and current measurements. Measurements are displayed graphically and numerically on a computer monitor to allow real-time adjustment of operating parameters and to determine when the system has reached steady state conditions.

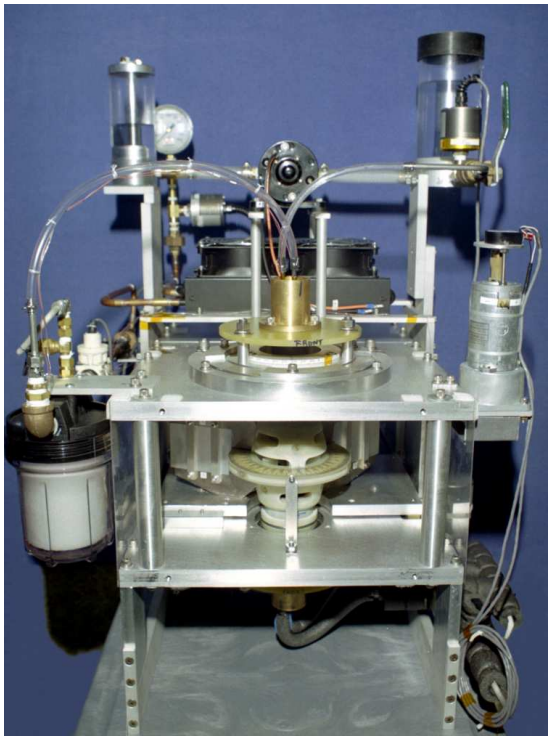

Figure 1.2: Rotating Bed Magnetic Refrigerator

Since originally completing the RBMR, we have improved the bed design and built additional bed wheels. The beds contain magnetocaloric material (MCM) in particle form. The beds are repackable so the same bed can be reused with different MCM's. We also built multiple interchangeable bed wheels of the latest design to speed the testing of different MCM's by allowing testing to continue with one bed while the next bed is packed with new material.

The heat transfer fluid is a solution of 10% ethylene glycol and 90% water to reduce the freezing point for low temperature RBMR testing. Checking the solution density before and after filling the RBMR ensured a correct, known solution.

1.2.2 Experimental technique.

The RBMR was used to explore the thermal performance of layering and first order magnetocaloric materials. The experimental protocol begins by first establishing a baseline performance of single layer AMR matrices using Gd, a GdEr alloy ($Gd_{0.94}Er_{0.06}$), a $Gd_5(Si,Ge)_4$ inter-metallic compound, and $La(Fe_{0.88}Si_{0.12})_{13}H_{1.0}$. The experimental plan includes 72 data points per magnetocaloric material to explore the dependence of temperature span on swept volume ratio, rotational frequency, cooling power, and thermal sink temperature.

Each load test curve consists of four heat loads for a given flow rate, rotational speed, and hot heat sink temperature. Data points are recorded at the maximum heat load (zero temperature span) and the maximum temperature span (zero heat load), and two additional points evenly spaced between those extremes. In the experimental plan, each material is tested at two hot heat sink temperatures, three rotational speeds, and three flow rates. Data

from the experiments were analyzed to determine the relative effects of flow rate, rotational speed, hot sink temperature, and cooling load upon temperature span.

An additional experiment known as a pseudo-magnetocaloric effect test examines the dependence of zero temperature-span cooling power on mean temperature. This test provides a good metric of the intrinsic performance of the magnetocaloric material as a refrigerant. In this test, the RBMR heat sink temperature is adjusted to produce zero steady state temperature span for points over a range of heat loads. The frequency and flow rate is kept constant, so there are two stable hot/cold temperature point pairs for each load value because of the dome-shaped curve. The resulting plot resembles a magnetocaloric effect (MCE) curve, with the peak heat load or cooling power occurring at the Curie temperature.

Since it is not possible to achieve exactly zero temperature span in the experiments, the heat sink temperature is adjusted to produce a slightly negative temperature span and then a slightly positive temperature span for a given heat load. Interpolating the average of the bed's hot and cold inlet temperatures between the negative span and positive span conditions gives the effective temperature at zero temperature span, which is plotted against the heat load.

In all tests, data is recorded after all system temperatures reach steady state, as indicated by no visible trend in temperature over the last five minutes. For every test point, 200 data points are recorded at 1.5 second intervals. All the data is collected in a spreadsheet and averaged and plotted to compare different operating conditions. The standard deviation is also calculated for the raw data to alert us to any parameter that may be varying more than typical.

The Gd-packed bed contains 161.6 grams of spherical particles sized 425 – 500 micron (-35 +40 mesh).

The GdEr-packed bed contains 164.0 grams of spherical particles sized 250 – 355 micron (-45 +60 mesh).

The GdSiGe-packed bed contains 183.3 grams of irregular particles sized 300 – 500 micron (-35 +50 mesh).

The LaFeSiH-packed bed (tested under a parallel NIST ATP program) contains 135.4 grams of irregular particles sized 246 – 500 micron (-35 +60 mesh).

The layered bed contains 85.6 grams of Gd and 82.7 grams of GdEr, of the same size used in the single-material beds.

All MCM's were tested in beds with the same total bed volume and length.

1.2.3 Evaluation of first order magnetocaloric materials in AMR.

Ames Laboratory provided the $Gd_5(Si_{2.09}Ge_{1.91})_4$ magnetocaloric material that we tested in the RBMR. $Gd_5(Si_{2.09}Ge_{1.91})_4$ is a material that was found by Ames to have a first order

magnetic transition around 9 C. We ground the material in air to reduce the particle size and sieved the material to produce quantity of irregularly shaped particles in the size range of 300 - 500 microns.

Tohoku University in Japan supplied the LaFeSiH material in the final powder form for a parallel program. We sieved the material to separate particles in the range 246 – 500 microns.

1.2.4 Evaluation of layering in AMR.

Based on RBMR test results with Gd beds and GdEr beds, we decided to use a 1 to 1 volume ratio of Gd to GdEr for construction of a layered bed. We assembled an additional bed based on our existing bed design, modified with mesh dividers in the middle of each compartment to separate the two MCM's.

1.3 Passive regenerator bed testing.

1.3.1 Description of PRS.

The passive regenerator system, designed and constructed under an earlier Navy contract, experimentally measures the ineffectiveness of passive regenerator beds. Passive regenerators exhibit most of the losses present in AMR's, except for those due to the magnetocaloric effect. During the passive regeneration portion of the AMR cycle, losses are caused by heat transfer resistance between fluid and solid, conduction from hot to cold ends of the matrix, and viscous flow dissipation. The combined effect of these losses is captured by regenerator ineffectiveness, which is the ratio of the steady state heat input to the product of heat capacity of the fluid flowing through the bed and the temperature difference across the bed.

$$iEh = Qh / (Vdot * rhof * Cf * (Th – Tc)$$

Where
IEh = regenerator ineffectiveness
Qh = heat input
Vdot = fluid flow rate
rhof = fluid density
Cf = fluid specific heat
Th = hot side temperature
Tc = cold side temperature

Passive regenerator beds can be fabricated from conventional materials such as stainless steel, separating the challenge of fabricating tight-tolerance geometric designs from the challenge of working with magnetocaloric materials.

The PRS uses a pump and solenoid valves to set up reciprocating flow in a pair of regenerator beds which are in series on either side of a flow-through electrical heater. The beds are placed adjacent to the heater and the whole assembly is insulated to prevent heat leaks from the heater to ambient, which would impact the ineffectiveness calculation.

Solenoid valves provide great experimental flexibility, allowing tests over a range of frequencies as well as enabling changes to the dwell ratio. The dwell ratio is the ratio of the amount of time when there is no flow, to the total cycle time. The dwell ratio is typically 1/3 in our experiments.

At one point, repeating earlier test points to check repeatability produced much higher ineffectiveness than before, and we noticed the temperatures were not symmetrical from one bed to the other. This lead to further tests which indicated the flow through the beds was unbalanced, i.e. not the same in both directions. The flow unbalance was traced to a small leakage through a malfunctioning valve.

Unbalanced flow of this type (more flow in bed A from cold to hot, and more flow in bed B from hot to cold) can increase ineffectiveness and also introduce error into our ineffectiveness measurements. We examined previous data sets and determined that only one series of data was collected while the valve was malfunctioning,

Replacing the malfunctioning valve rectified the unbalanced flow rates and temperatures, and the test results are again repeatable. The valve malfunction was caused by internal corrosion. We procured solenoid valves with an anti-corrosion coating to prevent future occurrence of the internal leakage that caused flow imbalance.

1.3.2 Experimental technique.

In typical PRS experiments the temperature controlled bath is set to 24 C, close to ambient temperature in order to minimize losses to the environment. The valve frequency and dwell ratio are set, and the pump is adjusted to produce the desired average flow rate. Then the heater power is adjusted to produce a 20 C average temperature difference across the beds. When the temperature span is steady, indicated by no visible temperature trend over a period of five minutes, 200 data points are collected at one second intervals. The data is tabulated and averaged in a spreadsheet for comparison with other test points.

In a typical test series, either the flow rate is held constant and the frequency is varied to explore the effects of changing R* ratio, or the flow rate and the frequency are both varied to maintain constant R* ratio and explore the effects of changing flow rate.

1.3.3 First advanced regenerator geometry.

One advanced regenerator geometry was identified in the Navy program as having a potential for efficient AMR performance in geometries readily fabricated by state-of-the-art technology. A set of regenerator components were fabricated in stainless steel at the conclusion of the Navy program.

Modeling indicated that certain arrangements of the advanced regenerator components produced better regenerator performance. This flow arrangement greatly improved heat transfer according to models.

The next passive regenerator bed we built has a modified version of the same advanced regenerator geometry. According to models, the heat transfer and pressure drop for this type of geometry is much less affected by geometric irregularities.

We conducted an additional series of passive regenerator experiments to determine if a slight non-symmetry in temperature that we observed between the two beds is caused by the beds themselves or the flow circuit and valves. The hot end of bed A was observed to be hotter than the hot end of bed B, and the cold end of bed A was also hotter than the cold end of bed B. The temperatures of the two beds were typically less than 0.5 C apart. This is much closer together than in the past when the valves were malfunctioning, but we still thought it could indicate unbalanced flow, and contribute to increased ineffectiveness. We suspected there was more flow from the cold end of bed B to the hot end, and thus more flow from the hot end of bed A to the cold end, than in the opposite direction. Since the heater is between the beds, this would heat up bed A.

Unbalanced flow could be caused by malfunctioning valves as has occurred in the past, or different pressure drops in different branches of the flow circuit, or different pressure drops across each bed in the tow flow directions. To determine if the source of the non-symmetric temperatures was the beds themselves or some aspect of the plumbing, we flipped the bed and heater assembly so bed A and bed B reversed positions relative to the flow circuit. If the flow circuit or valves were the cause, after switching positions bed B would be hotter. If the beds themselves were the cause, bed A would remain hotter. In repeated ineffectiveness tests with the beds reversed, bed A was still hotter than bed B, so it is the beds themselves that cause the non-symmetric temperatures in this case. Because the slight temperature imbalance in this case is due to the beds themselves we can not correct it with external adjustments.

1.3.4 Second advanced regenerator geometry.

We also developed and tested another advanced regenerator geometry passive regenerator bed. When we conducted ineffectiveness tests with this passive regenerator bed, the performance did not meet our expectations. Under the test conditions we expected ineffectiveness to be less than 1%, but the best (lowest) ineffectiveness observed during testing was 2.7%.

One of the underlying assumptions in the model is that the flow through the beds in both directions is balanced. Modeling suggests that a relatively small amount of unbalanced flow could cause substantial transport of heat across the beds and thus higher ineffectiveness. Unbalanced flow in this case means the amount of flow through the beds in one direction is not equal to amount of flow through the beds in the opposite direction.

We devised and conducted an additional experiment to determine if the flow is balanced in the PRS for these runs. In the experiment, the two outlet flows are collected in separate containers and weighed instead of being returned to the pump. Both outlet flows should be equal for a given period of time. But experiments indicate that there is significant flow imbalance under some conditions. The imbalance appears to correlate positively with switching frequency, ranging from less than 0.5% imbalance at 0.25 Hz cycle frequency,

up to 7% imbalance at 2 Hz. Flow imbalance could be caused by slight variation in the solenoid valve response time.

Modeling indicates that this type and amount of unbalanced flow can have a significant effect on regenerator performance. Since we suspect the flow may be imbalanced at high frequency, lower frequency test results are probably a better indication of true system performance.

1.4 Synthesis and characterization of magnetocaloric materials.

Ames Laboratory prepared three $Gd_{1-x}Er_x$ solid solution alloys with x = 0.02, 0.05 and 0.11 for the materials characterization part of the program, in addition to the $Gd_5(Si,Ge)_4$ provided for the RBMR test. Astronautics also provided to Ames pure Gd and a solution alloy ($Gd_{0.93}Er_{0.07}$) in a form of spherical powders prepared by the plasma rotating electrode process (PREP). These latter two were from the same batches of alloys as were tested in the Astronautics rotating bed magnetic refrigerator. Astronautics also provided two samples of Gd. This material is from one of the batches of material that was used in the SEP.

The materials were analyzed using x-ray powder diffraction and their magnetocaloric effects were calculated from magnetization data. All of the materials were prepared from commercial purity Gd and Er. Heat capacity was also measured for selected samples.

The isothermal entropy change dS was calculated from magnetization data using the following method, which assumes the Curie point of the material is already known approximately from DSC measurements. First an initial run of field sweeps is taken up to 2T, with temperature spacing of the data of 3 degrees, from about 20 degrees below the Curie point to 20 degrees above the Curie point. Then two more sets of field sweeps are taken with temperature spacing of 3 degrees, starting at temperatures offset by one degree and two degrees from the first set of data. Then the isothermal entropy change is calculated separately from each data set using

$$\text{DeltaS\_m} := \int_0^{\text{Hmax}} \frac{\partial}{\partial T} M(T,H)\, dH$$

,

and the three data sets from the temperature offset runs are plotted on a single scale to allow visual averaging to extract an accurate maximum value of dS.

Heat capacity curves were measured using an adiabatic heat pulse calorimeter from ~ 4 to 350 K in dc magnetic fields. The samples were cut in a rectangular shapes (4 x 4 x 10 mm) and weighed ~1.4 g. These measurements were carried out in dc magnetic fields of 0, 0.5, 1.0, 1.5 and 2.0 T.

The material used to make the MCM regenerator components in the SEP was pure Gd. Processing the material is challenging because Gd reacts strongly when heated with both oxidizing and reducing atmospheres, so the heating process must be done in the complete absence of oxygen, nitrogen, CO2, CO and water. We initially planned to install a layered bed in the SEP with both Gd and Gd-Er alloy MCM. The vendors were unwilling to quote on a large quantity of Gd-Er with a tight delivery schedule. Thus we were forced to use only Gd in the SEP.

The delivery schedule we requested for Gd exceeded the throughput capacity of the processing machine at the US-based production vendor. We thus split the order between two vendors, one that appeared to be using offshore production. The offshore production vendor was late on delivery and delivered material that appeared to be lower quality. Analysis of the material (see results section) showed that the contamination was not serious, but the geometrical irregularities may have adversely affected performance of the SEP. Clearly additional production facilities and perhaps new process development would be required if magnetic refrigerators were to be put into production using Gd in this geometry.

1.5 SEP testing.

1.5.1 Description of the SEP.

The subscale engineering prototype, or SEP, is a rotating magnet magnetic refrigerator (RMMR) device built for this project. The SEP is a flexible magnetic refrigeration test platform. The fixed beds can be individually instrumented, unlike a rotating bed design. A single bed can be removed for repair or replacement if necessary. The SEP uses a nominal 1.5 Tesla, dual field, permanent magnet to magnetize 12 stationary active magnetic regenerator (AMR) beds. The completed SEP is shown in Figure 1.3.

Figure 1.3: Completed SEP

The heat transfer fluid, water with a corrosion inhibitor, is controlled by four separate rotary disk valves. The valves are driven by the same motor that drives the magnet rotation in order to maintain correct valve phasing. The pump and the magnet drive motor both have variable speed drives to separately control the flow rate and cycle frequency. The machine has been operated at up to 5 Hz (150 RPM) and 3.5 LPM.

An in-line electric water heater provides the heat load on the cold side, and a brazed plate heat exchanger and a temperature controlled circulating bath controls the heat rejection temperature.

The SEP's open frame design allows access and space for instrumentation. The device has flow meters on the hot and cold sides, temperature and pressure sensors at the hot inlet valve, cold outlet valve, cold inlet valve, and hot outlet valve. There are also temperature sensors at the hot outlet of each bed, something that is not feasible in rotating bed designs. A novel drive system allows measurement of the drive motor output torque, including both the magnet drive and valve drive torque, or just the magnet torque or just the valve torque. There are also channels to measure drive motor, pump, and heater current and voltage, and a sensor to measure magnet rotational position and speed.

A high speed data acquisition system coupled to a PC shows data graphically and numerically in real-time, allowing monitoring and adjustment during experiments.

The tubes connecting the cold inlet valve and the cold outlet valve to the beds are isolated from ambient by an enclosure that surrounds those tubes beneath the bed mounting plate. The tubes connecting those valves to the cold heat exchanger are insulated with close-cell pipe insulation. The heater that makes up the cold heat exchanger is well insulated by closed-cell building insulation. The beds themselves are not insulated, as insulation would occupy too much valuable magnet gap volume. The hot side plumbing is not insulated for the most part, as the hot side typically operates close to room temperature, and there are temperature sensors at the hot inlet and outlet valves. The tubing between the hot heat exchanger and the hot inlet valve is insulated to aid in controlling the hot inlet temperature when it varies significantly from room temperature.

1.5.2 Experimental technique.

The main experimental technique used with the RMMR is similar to that used for the RBMR. Load curves consist of four heat loads ranging from the maximum load, which produces zero temperature span, to zero load, which produces the maximum temperature span. Load tests begin with the maximum load point, with the load adjusted to reduce the temperature span to within 0.5 C of 0 C. After that point is recorded, the heat load is reduced to 2/3 the initial value, then 1/3, and finally zero. For each heat load, once the temperatures have reached steady state, a series of 1000 data points are recorded over a period of one second. The average and standard deviation of each measurement is calculated in a spreadsheet.

1.5.3 Measuring individual bed pressure drop.

Before installing the beds in the SEP, we measured the pressure drop across each bed. The PRS is an excellent test stand, having a pump, accumulator, flow meter, pressure transducers, and valves to control flow direction. The pressure drop was measured for two flow rates in both directions for each bed. There is more variation in pressure drop between the beds than we hoped for, as shown in the results and discussion section.

1.5.4 Testing full SEP.

1.5.4.1 Range of operating parameters.

The SEP load test grid consists of three rotation speeds from 60 RPM to 120 RPM, three flow rates from 1 LPM to 3 LPM, and two hot inlet temperatures, 24 C and 36 C.

The device operates smoothly down to 60 RPM (2 Hz cycle frequency). 120 RPM (4 Hz) is close to the original design speed, but the SEP has been operated at up to 150 RPM (5 Hz). The currently installed drive motor can operate the device at up to 250 RPM (8.3 Hz).

The range of flow rates was chosen because the pump does not provide smooth flow much lower than 1 LPM, and the pressure above 3 LPM is approaching the structural limit of the beds. The device was designed for higher flow rate, but the higher-than-expected pressure drop in the beds limits the flow rate. While the beds were individually pressure tested on the bench to 50 psi with air, in the SEP they are subjected to the extra stresses of cyclical pressure loading and additional cyclical magnetic forces.

After the initial test grid was completed, we began experimenting with higher flow rates. However, at 3.5 LPM one of the beds developed a leak. The bed was removed and repaired, but the leak showed that we were approaching the pressure limit of the beds. Later, another bed developed a leak at 3.2 LPM and again removed and repaired.

The pump we specified for the SEP also began to overheat at the higher flow rates and pressures. We installed an alternate pump with slightly higher performance that was adequate to complete the experiments that were possible within the pressure limits of the beds.

1.5.4.2 SEP flow instrumentation

The SEP has two flow meters, one on the hot side before the hot inlet valve, and one on the cold side before the cold inlet valve. The two flow meters should indicate the same flow rate at all times, but the cold flow meter typically reads lower, sometimes by as much as 40% or 1 LPM. This could indicate a problem with the flow meters, or that some flow is bypassing either the beds or the cold heat exchanger.

The flow meters and pressure transducers show that substantial flow and pressure pulses occur in the SEP. Excessive pulsation could cause the flow meters to read incorrectly. After improving the design of the accumulator in the system to absorb pulses from the pump, experiments show that the remaining pulses are due to the valves switching.

1.5.4.3 Load testing.

The complete load test grid consists of three rotation speeds, three flow rates, and two hot side temperatures: 1, 2, and 3 LPM; 60, 90, and 120 RPM; and 24 and 36 C. For each set of parameters, we recorded four data points with the load ranging from zero load up to the load that produces zero temperature span. The grid ranges from the lowest practical speed and flow rate to the design speed and the highest practical flow rate. Because the pressure drop in the beds is higher than anticipated, we limited the flow rate in order to limit the pressure exerted on the beds.

The range of speeds and flow rates explored in the tests is wide enough to show that we exceeded the optimum flow rate at the lowest speed. This illustrated by performance that is better at 60 RPM with 2 LPM than with 3 LPM (or 1 LPM). At 90 RPM, the flow rate does not make much difference. At 120 RPM, the highest flow rate produces the best performance, indicating that more flow might produce more cooling power and greater temperature span.

In general, the SEP has good cooling power, even exceeding predictions in some cases, but the temperature span is disappointing. We suspect that regenerator geometry variation within the beds and differences between the beds is the major reason for the low performance.

1.5.4.4 Efficiency testing.

The total drive torque was measured for each SEP load test. The torque, along with the magnet speed measurements, allows calculation of the shaft work input. The total flow rate and pressure measurements allow calculation of pump work. The electrical heat load measurement allows calculation of cooling power. Calculating the work input this way neglects the inefficiency of the drive motor and pump. The ratio of cooling power to input power is the coefficient of performance, or COP. In the load tests the COP based on work input ranges from zero at zero load up to 13 W/W at zero temperature span.

The drive motor and pump current and voltage were also measured for the load tests. The electrical COP is much lower, ranging up to 2.8 W/W.

Calculated either way, the COP includes the drive friction in the valves and the rest of the drive train. These losses were higher than expected. The electrical COP includes the flow work in the entire system, including the filter and hot heat exchanger. Because of the pressure sensor placement, the flow work-based calculation does not include the pressure drop in those components. More details and data on efficiency are in the results and discussion section.

2 Results and Discussion

2.1 Rotary bed magnetic refrigerator experimental results.

2.1.1 Baseline materials in AMR

The three magnetocaloric materials (Gd, $Gd_{0.94}Er_{0.06}$, $Gd_5Si_{2.09}Ge_{1.91}$) screened for this project were tested in the RBMR over a range of flow rates, frequencies, temperatures, and heat loads, comprising a test matrix of over eighty measurements for each material. This baseline screening allows comparing the performance of different materials over a range of consistent conditions. $La(Fe_{0.88}Si_{0.12})_{13}H_{1.0}$ (LaFeSiH) became available after the conclusion of the MCM tests in this program, and was tested on a parallel NIST ATP program, with the results reported here for comparison.

We also completed “pseudo-magnetocaloric effect” tests for each material. The pseudo-MCE test shows the zero-span cooling power as a function of temperature. This test, along with the conventional load tests, helped our understanding of Gd and GdEr performance before constructing the layered bed.

For the most part typical AMR performance was observed. For example, increasing flow rates led to increases in both cooling power and temperature span at relatively high rotational speeds, as clearly shown in Figure 2.1 for the Gd bed. For a given flow rate, there is a crossover effect with temperature span. The temperature span is larger when the hot heat sink (bath) is warmer for the low heat load points, while at higher load points, the temperature span is larger when the hot heat sink is cooler. This is because the beds work best when they are operating near the Curie temperature, which is approximately 20 C for Gd. When large heat loads cause a small temperature span, the bed produces a larger temperature span for a given load when the bath temperature is 20 C, and the entire bed is

close to the Curie temperature. For small heat loads and large temperature spans, the beds operate better when the bath temperature is 25 C because the average bed temperature is closer to the Curie temperature than it would be with a 20 C bath. For example, when the temperature span is 10 C and the bath is 25 C, the average bed temperature will be close to 20 C.

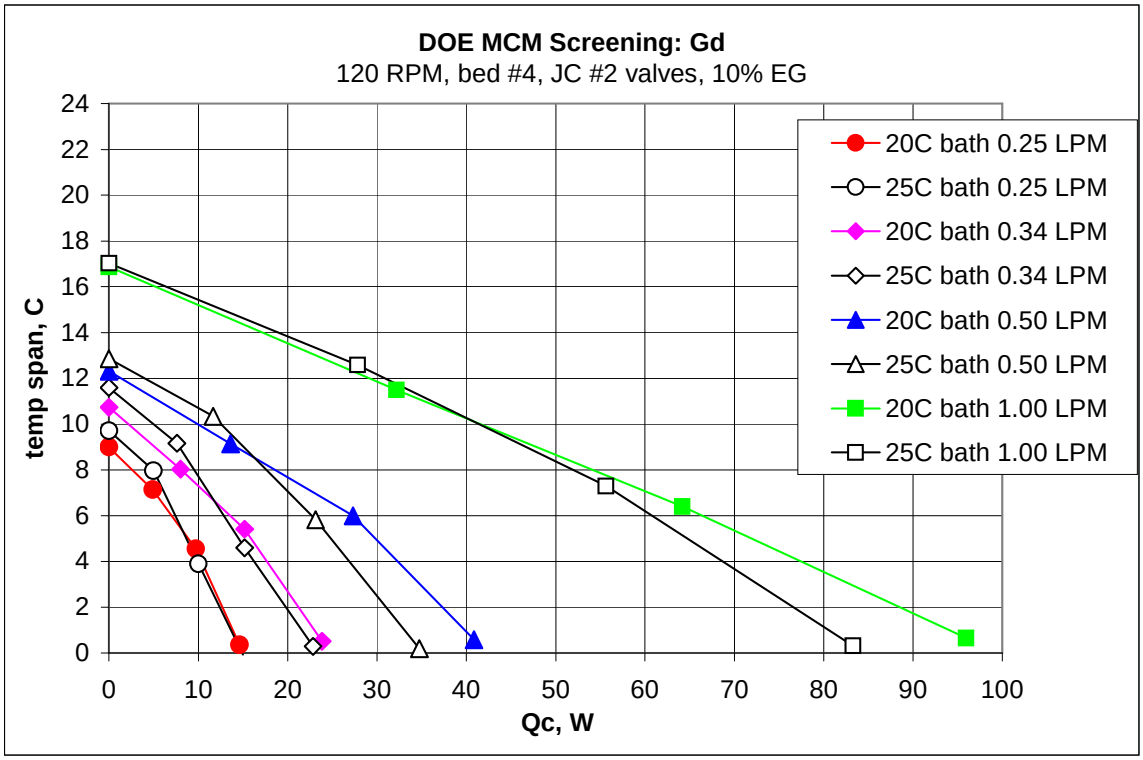

Figure 2.1: Gadolinium bed load tests

Figure 2.2 shows the effect of rotational speed on cooling power and temperature span. The flow rate is held constant for these tests while the rotational speed is varied, thus varying the mass flow through each bed per cycle, or the utilization factor (R* ratio). The beds function better for higher temperature spans at higher rotation rates. Conversely, at the highest load point the highest rotation rate produced a smaller temperature span. This is a result of the tradeoff between finite bed heat capacity effects during fluid flow and heat transfer losses during magnetization/demagnetization. At low frequencies, the large amount of fluid passing through the bed during each cycle is a significant fraction of the heat capacity of the solid matrix, and the resulting movement of the temperature profile in the bed allows some heat to flow to the cold side of the bed, reducing the net cooling power. This effect is most significant at large temperature span. At high frequencies, losses are generated by heat transfer between the rapidly magnetizing and demagnetizing bed particles and the pore volume heat transfer fluid. This loss at 240 RPM appears to override the effect of the finite bed heat capacity at very small temperature span. Thus at high span, the best performance is obtained at high frequency because of finite bed heat capacity effects, and at low span the best performance is obtained at moderate frequency because of heat transfer losses during magnetization/demagnetization.

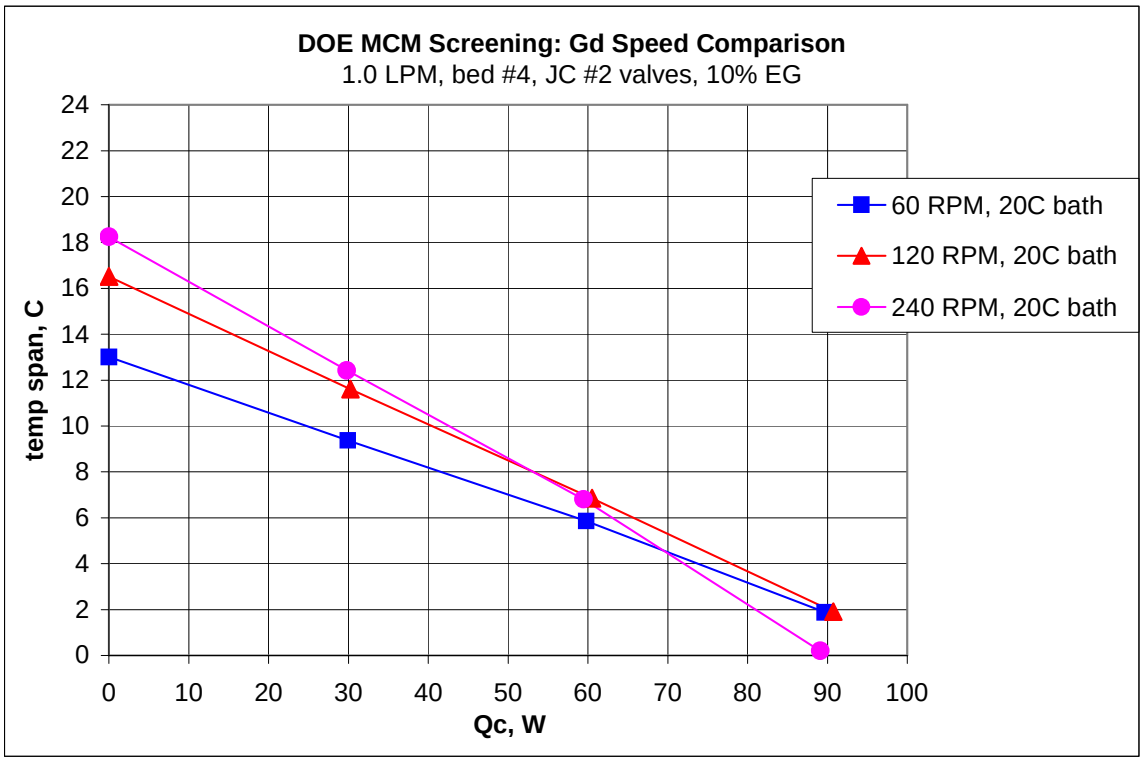

Figure 2.2: Gd bed load test: speed comparison

To further investigate how Gd performance depends on temperature, load tests were conducted with four different hot heat sink (bath) temperatures (with the same flow rate and rotation speed). As shown in Figure 2.3, for a given cooling power the temperature span is larger when the bath temperature is closer to the Curie temperature. In this series of tests, the beds produced the largest temperature span with the bath set to 20 C. The performance gap between different bath temperatures narrows at the lower load points because as the temperature span increases with decreasing load, the mean bed temperature declines. This brings the mean temperature closer to the Curie point (20 C) for the higher bath temperature cases, and pushes the mean temperature below the Curie point for the 20 C and 25 C cases.

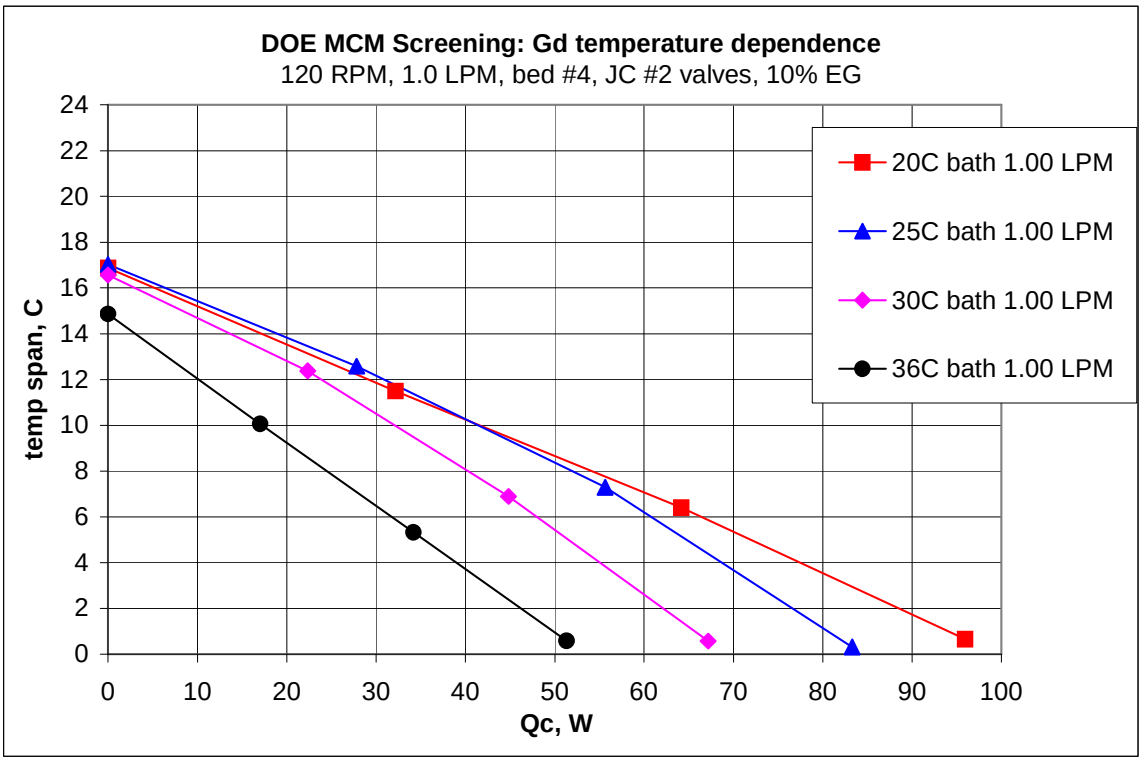

Figure 2.3: Gd temperature dependence

Figure 2.4 shows similar load test data for $Gd_{0.94}Er_{0.06}$ (GdEr). Again, the temperature span and cooling power are higher for the higher flow rate. Also similar to the Gd data, for a given flow rate, the temperature span is higher at large heat loads when the heat sink (bath) temperature is closer to the Curie temperature, in this case approximately 8 C for GdEr. The temperature span is again larger at low cooling power when the bath is 25 C, thus making the average bed temperature closer to the Curie temperature.

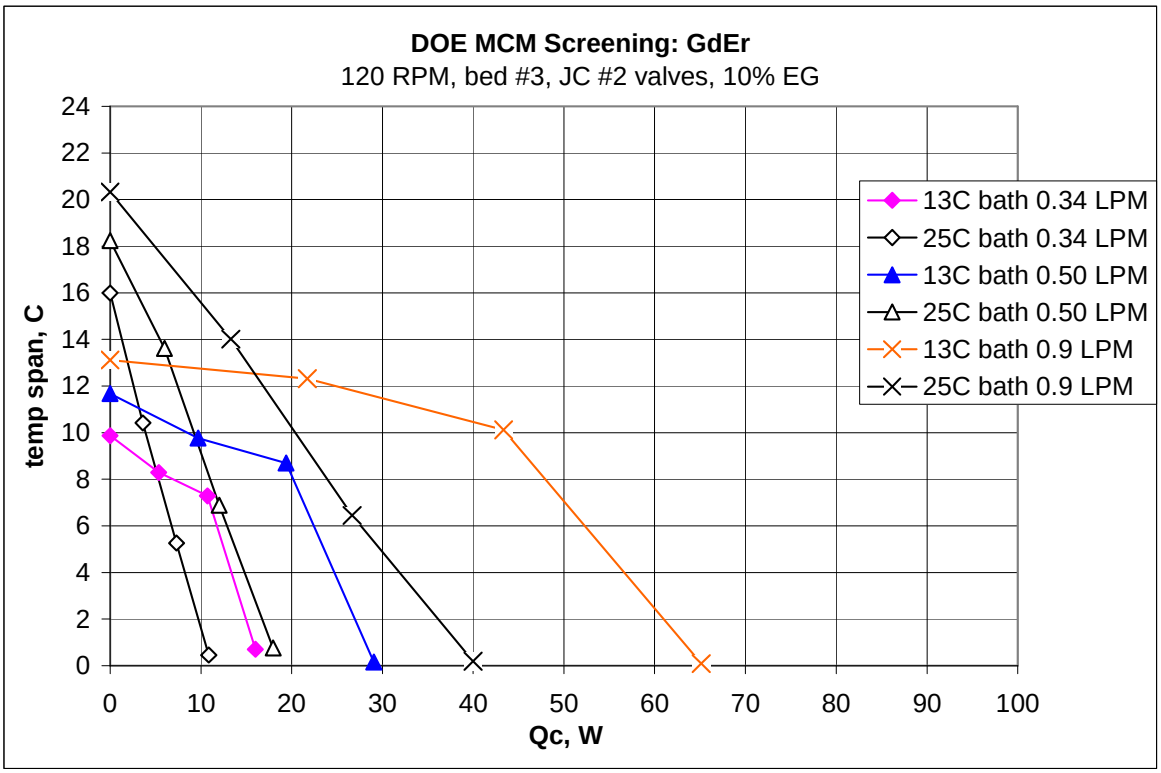

Figure 2.4: GdEr bed load tests

2.1.2 First order magnetocaloric materials in AMR.

The standard load test grid consists of tests at 60 RPM, 120 RPM, and 240 RPM, but the $Gd_5(Si_{2.09}Ge_{1.91})_4$ material produced little cooling power at higher speeds, in contrast to the other tested materials. To explore the frequency dependence, we measured the no-load temperature span over a range of speeds and flow rates. Figure 2.5 shows the temperature span declining with increasing speed. Depending on the bath (hot heat sink) temperature and flow rate, the temperature span peaks between 30 and 90 RPM, before losses start to overcome the cooling power.

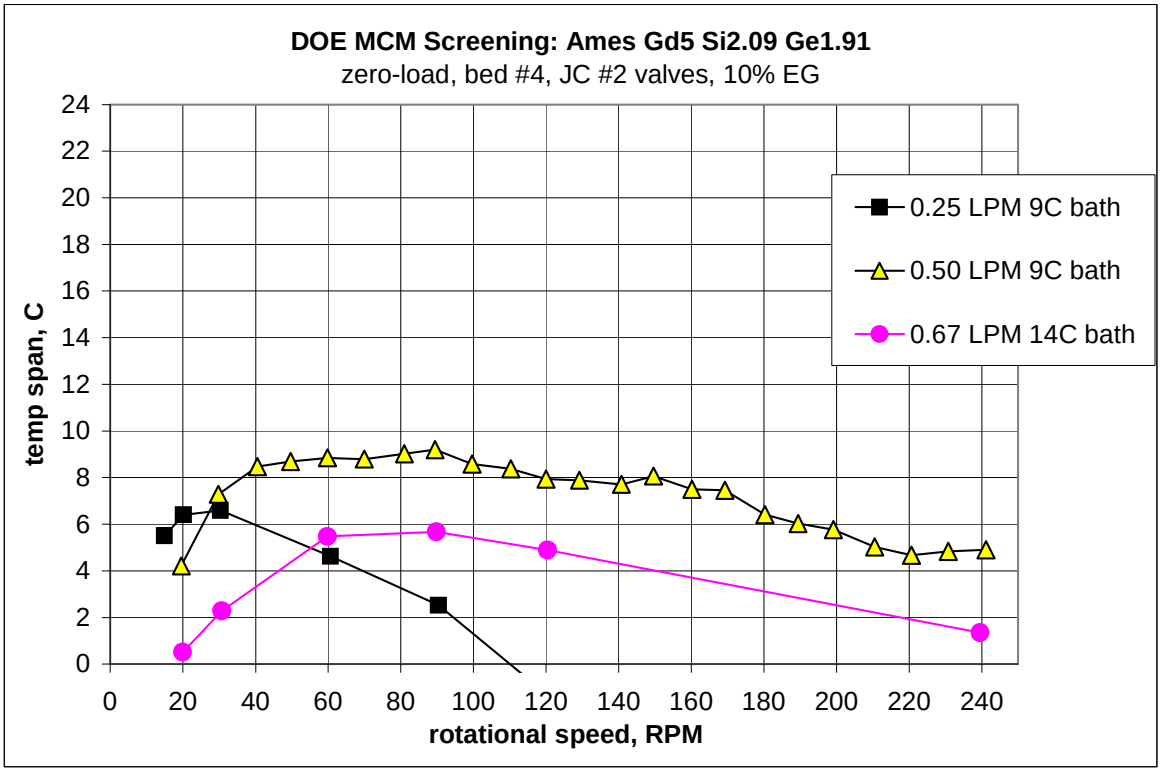

Figure 2.5: GdSiGe frequency dependence

Complete load curves taken at the same flow rate and bath temperature but different rotation speeds in Figure 2.6 show how much the cooling power depends on speed. Doubling the speed from 60 RPM to 120 RPM reduced the maximum cooling power from approximately 17 W to 11 W.

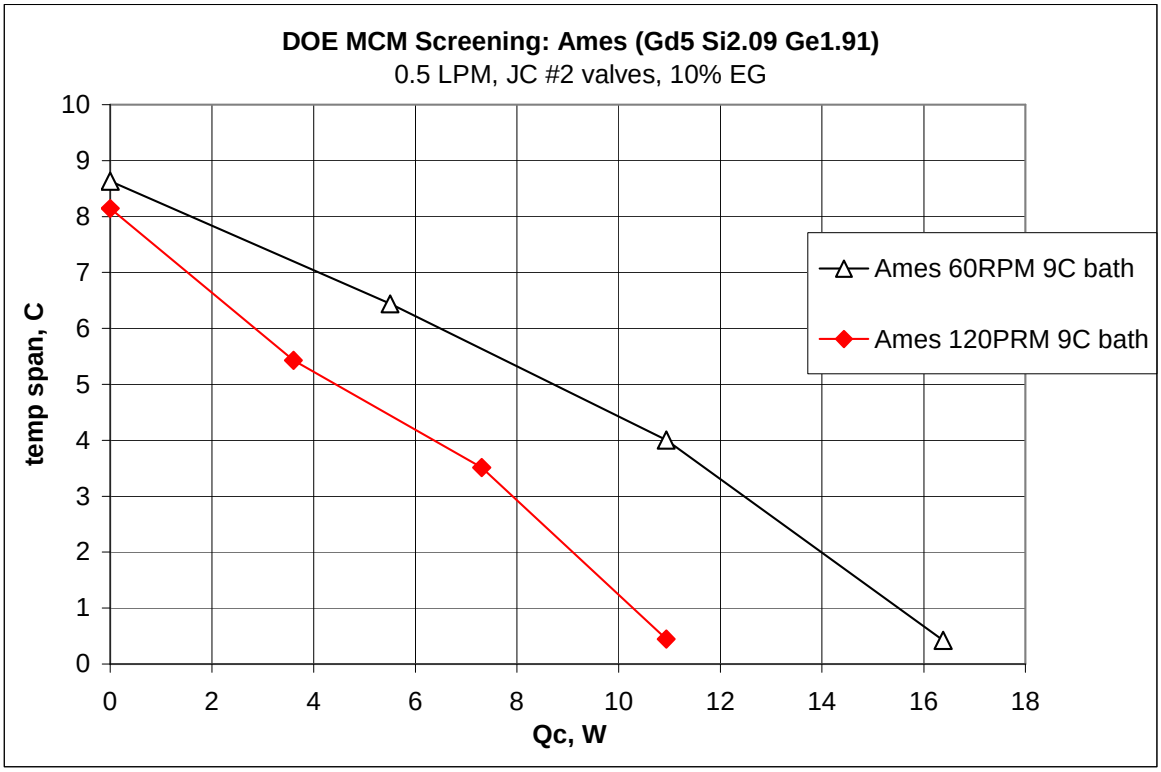

Figure 2.6: GdSiGe load tests at two frequencies

The frequency dependent effects may be related to the GdSiGe material's first order phase transition. There may be hysteretic heat generation upon rapid magnetization and demagnetization, or the large magnetocaloric effect might fade away at higher frequency if the first order coupled structural-magnetic phase transition in this material does not occur fast enough. These are the first measurements of a first order material in a rotary magnetic refrigerator which has the capability to probe the frequency dependence of the materials beyond 1 Hz, but the measurements should not be used to predict the performance of other first order phase transition materials. Moreover, not all first order materials have the same type of phase transition. For example, the $La(Fe_{1-x}Si_x)_{13}H_y$ series of materials have a first order magnetic transition that has a volume change, but no structural symmetry changes, and the frequency dependence of this compound appears to be quite different.

We also determined that the GdSiGe material works better at or below its Curie temperature of approximately 9 C. We tested other magnetocaloric materials at and 5 C above their Curie temperatures. The next figure (2.7) compares load tests for three materials at 60 RPM and 0.5 LPM. Gd and GdEr were tested with 25 C and 13 C bath (hot heat sink) temperatures, respectively, each 5 C above their respective Curie temperatures. We tested GdSiGe at 14 C, also 5 C above its Curie temperature. Compared to Gd and GdEr, the GdSiGe hardly produced any cooling power at all at the 14 C bath temperature. The GdSiGe performed better in further tests at lower bath temperatures. We observed the largest no-load temperature span with 5 C and 9 C baths, while 1 C and 5 C baths produced the most cooling power. The RBMR was not designed for operating much below 0 C, so the difference in performance between the 1 C and 5 C curves at no load may partly be due to water condensation on cold parts of the mechanism.

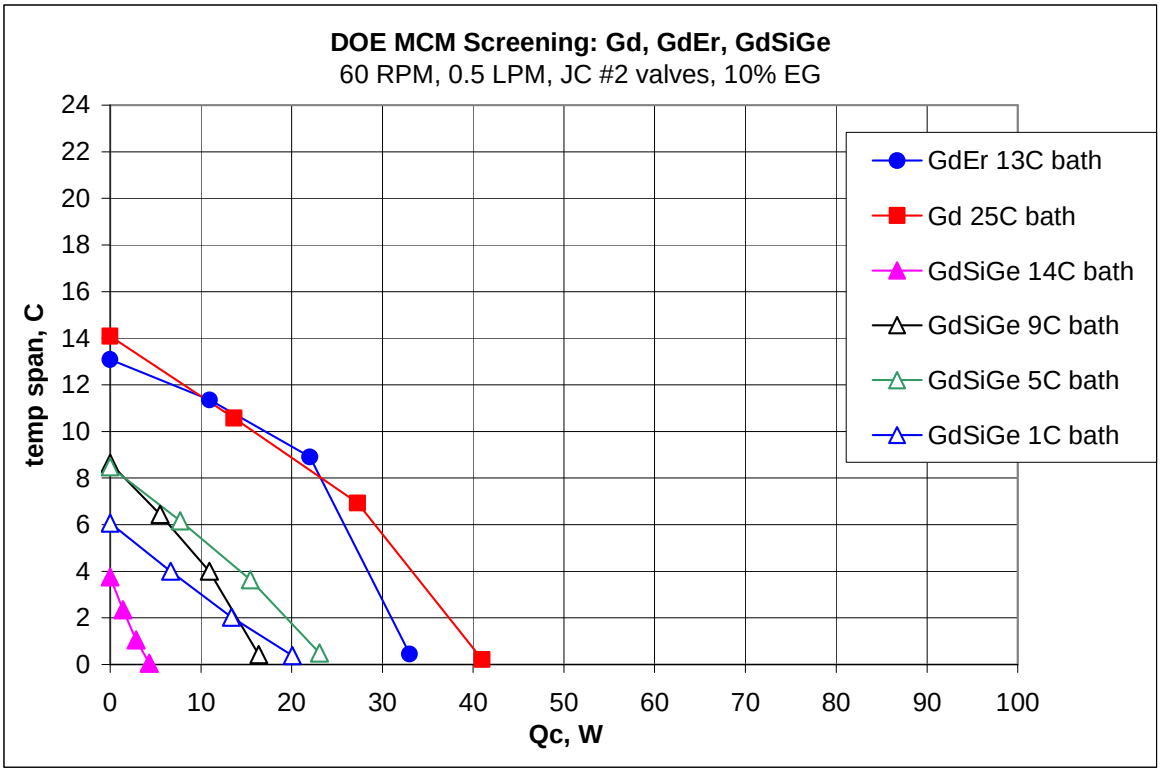

Figure 2.7: GdSiGe temperature dependent load tests

We also tested another first order MCM in the RBMR, LaFeSiH from Tohoku University, under a parallel NIST ATP program after the conclusion of the RBMR testing in this program. The load curves for this material have a pronounced knee shape, as shown in Figure 2.8. The GdEr packed bed produced similar results when operated at temperatures close to its Curie temperature. The LaFeSiH performance does not decline with increasing cycle frequency as it does with GdSiGe.

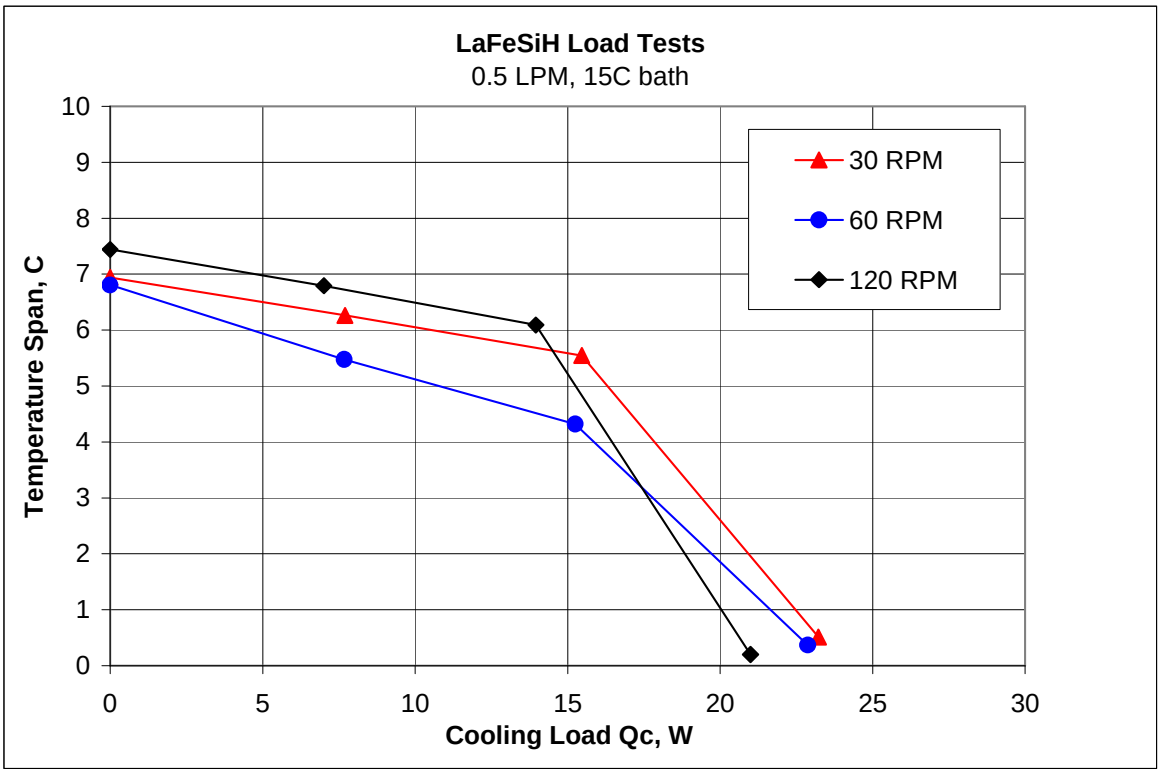

Figure 2.8: LaFeSiH load tests

2.1.3 Layering in AMR.

We also built and tested a bed with both Gd and GdEr layered in a 1 to 1 ratio. Test results are encouraging, with the layered bed performing better than the Gd-only bed and the GdEr-only bed. Figure 2.9 shows load test curves for Gd, GdEr, and the layered bed at 120 RPM and 0.5 LPM. We typically set the hot heat sink to 5 C above the Curie temperature for each bed, so the bath is 25 C for the Gd bed, 13 C for the GdEr bed, and we picked 5 C above the average of the Curie temperatures, or 20 C, for the layered bed. The layered bed produces more cooling power at zero span, and a higher temperature span at zero load than either of the other beds.

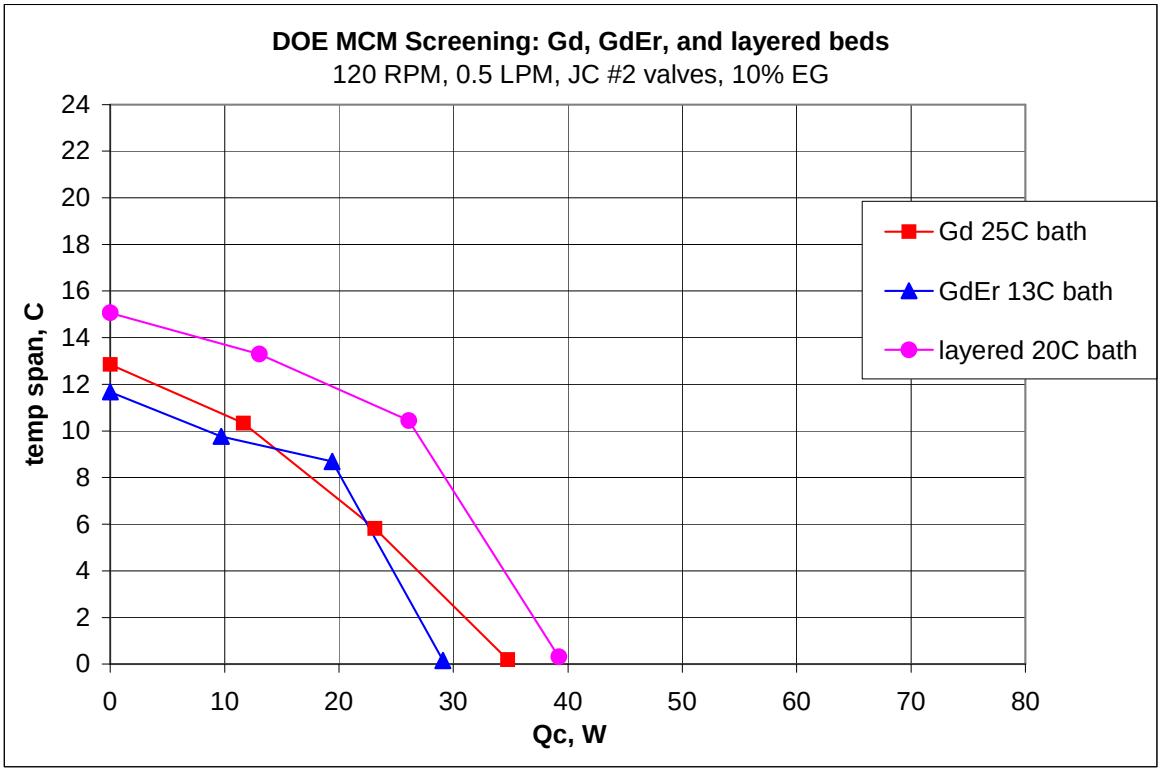

Figure 2.9: Gd, GdEr and layered compared at 120 RPM

The shape of the layered bed load curve is between the shapes of the single material curves. The Gd curve is fairly straight, while the GdEr curve has a knee. The layered bed curve has more of a knee than the Gd curve, and is straighter than the GdEr curve.

The following figure (2.10) shows similar load tests for the three beds at 240 RPM and 0.67 LPM. The results are similar, with the layered bed producing more cooling power and a larger temperature span. At this speed and flow rate the differences in maximum cooling power are less pronounced than at the lower speed and flow rate. The shapes of the various curves are similar to the previous plot.

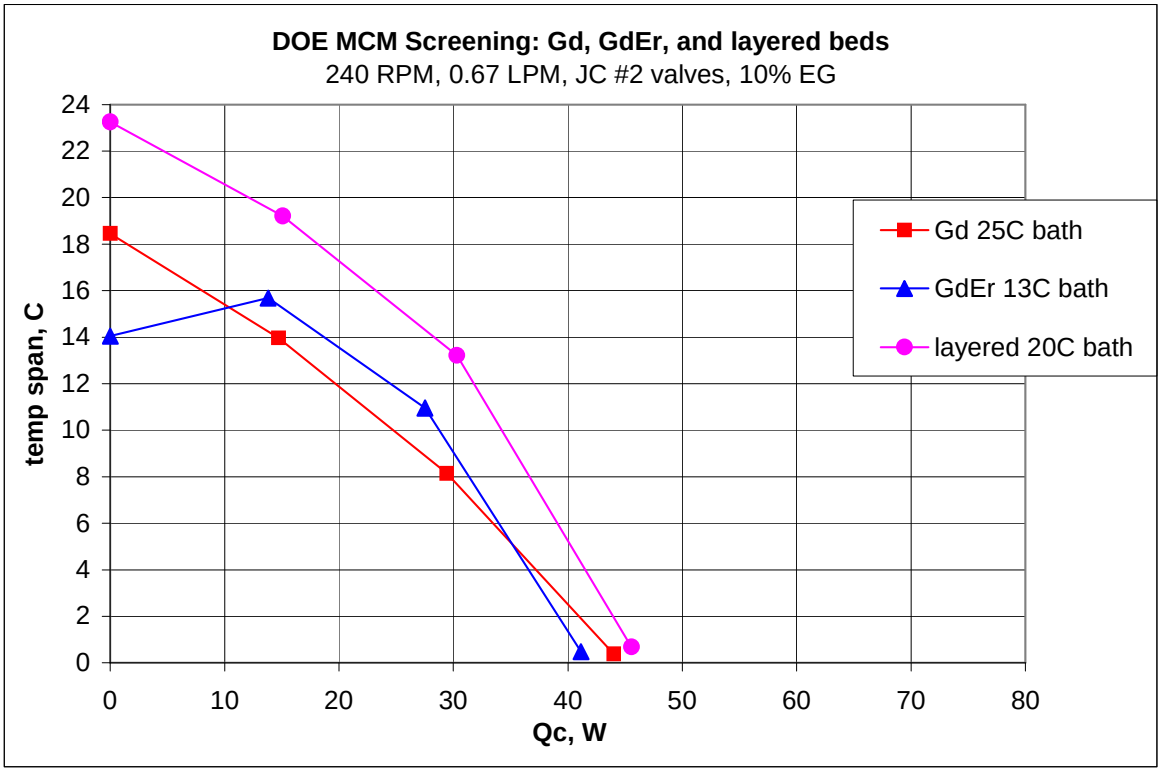

Figure 2.10: Gd, GdEr and layered compared at 240 RPM

Another way to compare the two individual MCM beds with the layered bed is by fixing the hot heat sink at the same temperature for all three beds. This case is illustrated in the next figure (2.11), where we conducted load tests for all three beds with the cold bath set to 25 C. This is a more realistic comparison, because any practical device would have to reject heat at a specific temperature regardless of what MCM it utilized. With the same heat sink temperature, the Gd bed produced the same cooling power at zero span as the layered bed. At no load, the GdEr bed has a larger temperature span than the layered bed. But in between those two extremes, the layered bed has a significant advantage. For instance, the layered bed produces almost 20 W of cooling power at a nearly 12 C span, while the Gd bed produces only 5 W at that span, and the GdEr bed produces about 8 W. Alternately, the Gd bed only has a 7 C span at 20 W, and the GdEr bed can not even produce 20 W of cooling power under these conditions. Thus, where a real device needs to operate most of the time, between maximum cooling power and maximum temperature span, the layered bed illustrates a clear advantage over a bed consisting of either one of the constituent materials alone.

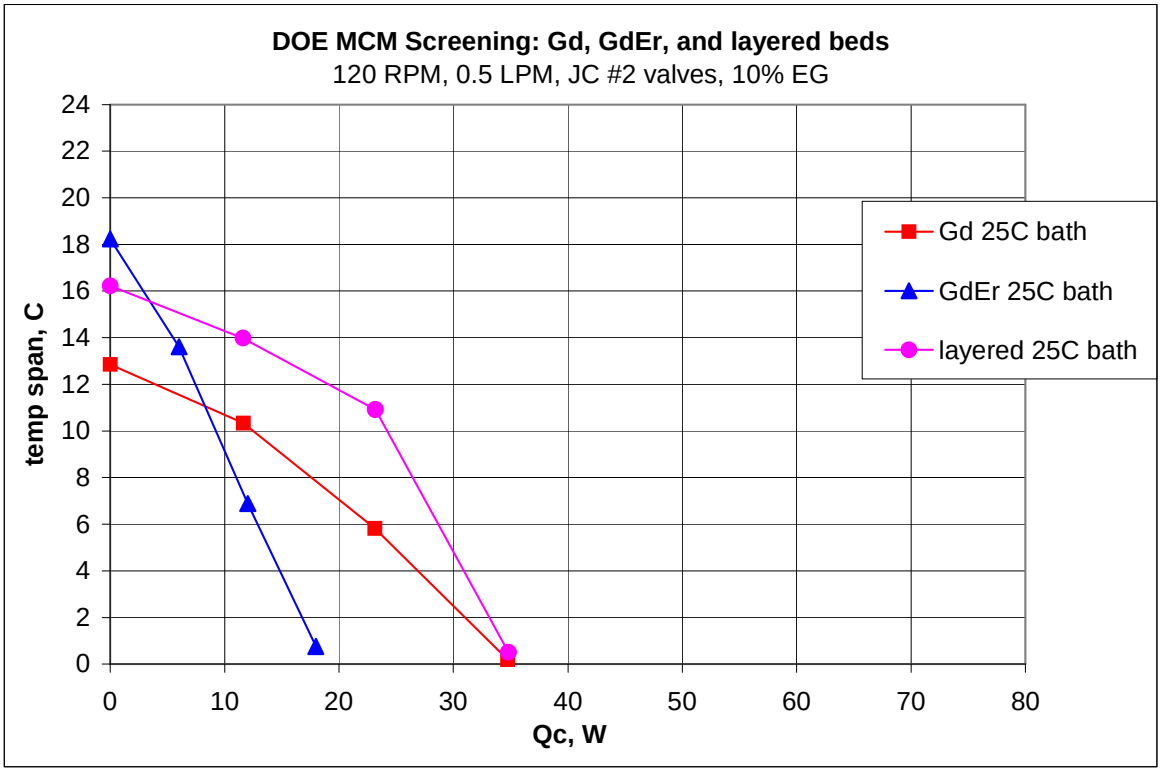

Figure 2.11: Gd, GdEr and layered bed compared with 25 C hot heat sink

In another series of layered bed tests, we conducted load tests with the bath (hot heat sink) set to increasingly high temperatures, as shown in the next figure (2.12). The maximum temperature span corresponds directly with bath temperature, with the highest bath temperature producing the largest temperature span, in this case the 43 C bath resulting in a 19 C span at no load. The lowest bath temperature, 20 C, produced the smallest temperature span, 15 C. The situation is reversed for maximum heat load at zero span. Here the highest bath temperature resulted in the lowest heat load. The bed produces the most zero-span cooling power with the lowest bath temperature because that temperature, 20 C, is closest to the Curie temperature of the bed constituents. With zero span the whole bed is at one temperature, so at higher bath temperatures the bed moves away from the Curie temperature where it functions best.

It is interesting to note the shapes of the load curves. When the bath temperature is higher the curve is straighter, more like load curves for Gd beds. With lower temperature baths, the curves have a “knee” shape more like curves for GdEr. This is because the entire bed is above the Curie temperature of Gd at the higher bath temperatures, and the GdEr portion of the bed does not have much effect on performance. The opposite is true at the lower bath temperatures. With the bed below the Curie temperature of Gd, the resulting load curve looks more like those produced by a GdEr bed, because that is the portion of the bed producing most of the cooling.

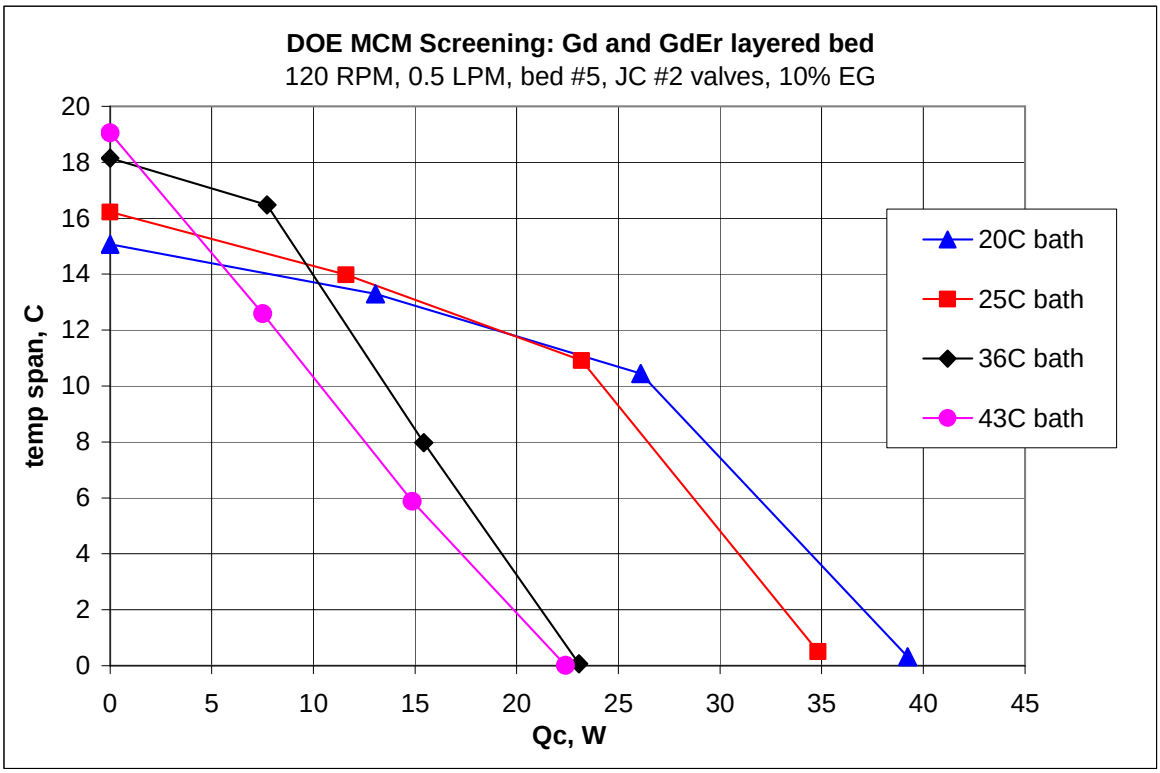

Figure 2.12: Gd and GdEr layered bed at different hot heat sink temperatures

In “pseudo-magnetocaloric effect” tests, plotting the heat load at zero temperature span versus average bed temperature approximates the shape of the magnetocaloric effect curve, where the largest cooling power is expected to be attained at the Curie temperature.

Figure 2.13 shows the pseudo-magnetocaloric effect test results for five beds. These results exhibit the general character of a peak centered in the region of the Curie temperature of the material.

The cooling power peak for Gd is in the range of 15 to 19 C according to the experiment, corresponding to the 16 C Curie temperature we measured for this batch of material at 1.5 T. The test becomes difficult to perform in the region near the maximum cooling power. This is partly because when the cooling power is at maximum, the cooling power and temperature span are insensitive to changes in average temperature, which is the means used to interpolate to zero span. Attaining equilibrium also becomes more sluggish in this region where the heat capacity of the magnetocaloric material is at a maximum.

The GdEr cooling power curve has a similar shape, with the peak is near 7 C, close to the expected Curie temperature of 8 C.

The observed GdSiGe peak in cooling power occurs between 6 and 7 C in the experiment, close to the expected Curie temperature of approximately 9 C. The points for the GdSiGe were not interpolated to zero span between slightly positive and slightly negative temperature difference points like the other materials, and instead are points that are close

to zero span but slightly positive. This makes the pseudo-MCE curve magnitude slightly lower than it would otherwise be.

Compared with curves for beds containing just Gd and just GdEr, the curve for the bed layered with Gd and GdEr does fill in the "valley" between the two single MCM bed peaks. Under these specific test conditions, the layered bed curve does not exhibit dual peaks of its own, but instead produces a broader peak than either of the two single MCM beds. The peak cooling power for the layered bed is lower than the Gd bed peak and slightly higher than the GdEr bed peak. However, the layered bed does produce less cooling power at the temperatures where the two single layer beds have maximums. The layered zero span performance may be hampered because only one of the layers provides much cooling power at these points, or there may be a loss associated with the interface between the two MCM's in the bed. However, at moderate temperature spans, the layered bed provides greater cooling power than beds made from either of the two component materials.

The LaFeSi cooling power peaks at 11 C, right at the 11 C Curie temperature at 1.5 T, and the peak is much sharper than any of the other materials.

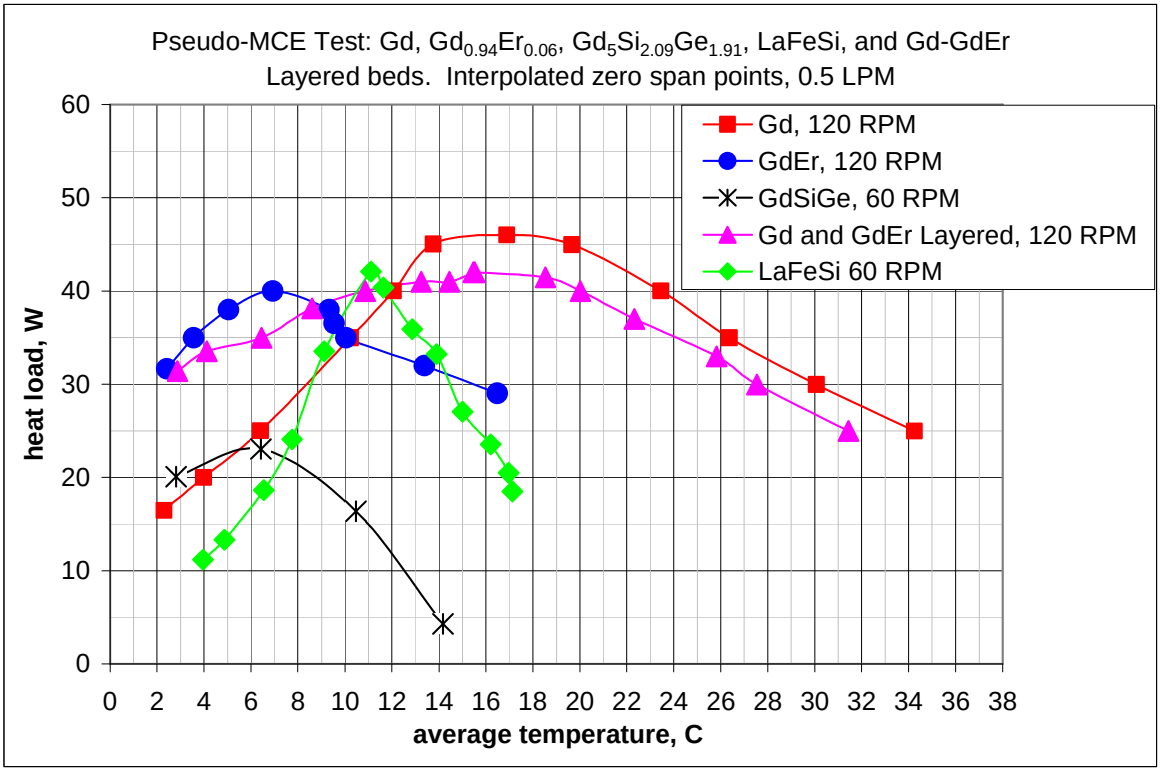

Figure 2.13: Pseudo-MCE test

2.2 Passive regenerator test results.

The main goal when designing a MCM bed is to minimize the volume while achieving target performance. Minimizing MCM volume reduces the cost associated with the MCM itself, but more importantly it reduces the volume of the magnet gap where the bed must

fit. The magnet volume and mass, and thus cost, are proportional to the magnet gap volume. The magnet is a major cost component of a magnetic refrigeration system, so minimizing its cost is important.

Passive regenerator testing provides a means to explore advanced geometry regenerators using conventional materials and fabrication techniques. The losses incurred in the regeneration portion of the active magnetic regenerator cycle are also present in a passive regenerator: flow work, longitudinal thermal conduction, and solid-fluid heat transfer losses. Experimentally measuring ineffectiveness is a way to compare the performance of different candidate regenerator geometries.

We conducted ineffectiveness tests with six different passive regenerator geometries: spherical particles, irregular particles, screens, the first advanced regenerator geometry (PRS1, PRS2), the modified first advanced regenerator geometry (PRS3), and the second advanced regenerator geometry (PRS5).

The bed packed with stainless steel spherical particles provides a baseline to compare with model results using known correlations. This bed is re-packable, so different size and shape particles can be compared in the same bed.

The screen beds each contain 1000, 1 inch diameter, 200 mesh stainless steel screens. This highly effective regenerator confirmed that the PRS apparatus is capable of operating at low ineffectiveness. It is not practical to fabricate screens out of gadolinium due to gadolinium's tendency to work harden during drawing and its reactivity at annealing temperature.

The PRS1 bed was the first attempt at building an advanced geometry regenerator bed. Each bed is constructed from stainless steel regenerator components.

The PRS2 beds are similar to the PRS1 beds, except the beds are longer, and the regenerator components were more carefully screened in an attempt to reduce the variation in geometry.

In the PRS3 beds, the regenerator geometry is similar but was modified in order to reduce the bed's sensitivity to geometrical manufacturing and assembly tolerances.

The PRS5 beds are a different kind of advanced geometry. It is challenging to manufacture the small features necessary for high regenerator performance, so this design takes another approach to producing the small features.

The same bed housing used to test spherical particles was later packed with irregular steel particles. These particles pack with higher porosity than spherical particles, 47% versus 35%.

There are two typical types of ineffectiveness test series: varying the cycle frequency with constant flow rate to cover a range of R* (utilization) ratios, and varying the cycle frequency and the flow rate to maintain constant R* ratio over a range of flow rates. For all tests the heat load is adjusted to maintain a constant temperature span.

PRS3 advanced regenerator geometry bed test data illustrates typical regenerator ineffectiveness performance tendencies: performance improves (ineffectiveness decreases) with decreasing R* ratio, and for a given R* ratio, ineffectiveness decreases with increasing flow rate (and frequency).

To check ineffectiveness test repeatability, the same screen bed was tested at two flow rates before and after the solenoid valves were replaced. The results are fairly consistent, but the slight variations show that small differences in the results may not indicate a real difference in performance between different beds.

Comparing ineffectiveness test data for all of the passive test beds at 0.7 LPM for a range of R* ratios shows that as expected, the ineffectiveness increases with increasing R* ratio for all of the beds. Comparing the performance for PRS1, PRS2, and PRS3 illustrates that each successive advanced geometry regenerator bed design performed better, but the performance did not meet our expectations. As discussed in the modeling section, we suspect fabrication and assembly tolerance issues caused flow maldistribution and resulted in reduced performance. The other type of advanced geometry regenerator bed, PRS5, attempted to avoid tolerance issues using a different method to control flow channel size, but we suspect geometry variation again caused flow maldistribution and the resulting poor performance.

The screen bed exhibits the best regenerator performance, significantly surpassing the other beds. Unfortunately it is not practical to fabricate screens from promising magnetocaloric materials.

The irregular particle packed bed also performed well. This points to a practical near term method to produce a high porosity, high performance bed using the most promising magnetocaloric materials.

The same beds were also tested at constant R* ratio for a range of flow rates. The ineffectiveness decreases with increasing flow rate for all of the beds. Again, the initial type of advanced geometry bed performance improved with each iteration, but at best the ineffectiveness only reached the level of particle packed beds. The screen bed again achieved the best performance.

2.3 Advanced geometry regenerator bed fabrication.

2.3.1 First advanced regenerator geometry.

The first advanced geometry regenerator beds (PRS1) were assembled from stainless steel regenerator components produced by an outside vendor, and other components produced by Astronautics. Astronautics also designed and fabricated the necessary assembly fixtures.

An example of the stainless steel components was examined under scanning electron microscopy (SEM). The geometry was found to be very uniform, and the general shape of the features was as expected.

Additional components were examined by optical microscopy, which is a faster process. We again found that one aspect of the geometry was uniform, but another aspect varied between batches of components, and exceeded the specified value. The vendor revised their process to obtain components closer to our specifications in subsequent batches.

A second advanced regenerator geometry bed (PRS2) was assembled and tested. This bed has the same design as the first bed, but the components are from a single shipment to reduce variation. The components were also sorted more carefully to narrow the range of geometry variation due to manufacturing tolerance, compared to the first bed. This second bed is also twice as long as the first bed, which reduces the effect of dead volume in the plena.

According to FEA models and experiments, this bed geometry is sensitive to certain manufacturing and assembly tolerances. Using FEA modeling, we designed another bed geometry to reduce the sensitivity to manufacturing and assembly tolerance. This design uses similar geometry, but is arranged in a certain way to reduce sensitivity to tolerances.

2.3.2 Second advanced regenerator geometry.

Current fabrication technology sets an upper limit on feature size. An alternative regenerator geometry uses another method to produce the flow channels. This geometry can achieve smaller hydraulic diameter than the first advanced regenerator geometry.

Theoretical correlations were used in the AMR analytical model to perform a parametric optimization of regenerator operational and geometrical parameters, such as flow rate, cycling frequency, bed length, and internal bed feature size. The optimization results suggested similar flow rates, regenerator lengths, and cycling frequency for random packed particles and for both advanced regenerator geometries. However, the ordered geometries tended have to higher volumetric porosity and lower pressure drop across the regenerator than the random packed particles. The second advanced regenerator geometry achieves a specific cooling power at a 20% larger hydraulic diameter than first geometry. This suggests that fabricating second geometry would be easier than fabricating the first geometry.

We also performed analysis to determine if the strength of the bed assembly would be adequate. The boundary conditions for the bed are complex, so directly calculating deflection is challenging. We conducted modal analysis for some designs, and it appears that the natural frequency is high enough so deflection should not be a concern.

We considered multiple ways to fabricate this regenerator, concentrating on methods to produce precise, reproducible geometry.

One technique that initially looked promising used a process that is commonly used in industry, but had not been applied to the materials we needed to use. The company we talked to has the ability to produce very precise features, but because they do not normally use metals, getting their process to work in our application would require a very costly development program.

We ended up selecting a common industrial technique that Astronautics uses as part of our core business operations, in Milwaukee, Wisconsin. Using this machine appealed to us because we would have local control over the process. The machine is normally used for a somewhat different application, but leveraging our in-house expertise provided the opportunity for rapid design iterations and close control of the process.

The plenum design is critical to flow distribution, pressure drop, and dead volume. For this reason we decided to test passive regenerator beds with the same cross section and plenum design as the SEP beds. This way we expected to learn as much as possible about the bed design we planned to use in the SEP. This approach also meant we did not need to design separate plenums for the SEP and the PRS. Additionally, assembling the PRS beds served as a dry run for assembling the SEP beds. We also used the same assembly fixtures and tooling for both types of beds.

In parallel with the passive regenerator effort, we pursued building the SEP with gadolinium versions of the same geometry. The processing vendor completed a sample run of gadolinium components using the PRS/SEP design. The high yield alleviated one of our major concerns about the process.

We used the stainless steel components to assemble a pair of passive regenerator beds. Measurements show that we came close to our target values for the bed dimensions. Steady flow pressure drop experiments show that the two beds are more similar to each other than the first pair of beds we built. The difference in pressure drop between the two new beds is approximately 5%, compared to 25% for the previous pair of beds.

2.4 AMR modeling.

Modeling was done in this program to design the SEP and predict its performance. We also used the model to determine the size of components of a 3 ton magnetic air conditioner (3TMAC) in order to compare its cost to existing vapor cycle air conditioners. The model we used is a semi-analytical (SA) model developed by Astronautics before the start of the program, and refined under a parallel program and also as necessary under this program to perform the modeling of the SEP and 3TMAC.

Basics of the semi-analytical (SA) model

The Astronautics semi-analytical **(**SA) model of the AMR is based on a system of partial derivative equations describing the energy balance in a unit volume of the AMR bed. The governing equations are written separately for a solid regenerative matrix built of magneto-caloric material (MCM), and for the heat transfer fluid:

$$\frac{(1-\varepsilon)\cdot C_m}{P}\cdot\left(\frac{\partial T_m}{\partial t}-D_m\cdot\frac{\partial B}{\partial t}\right)=h\cdot a_w\cdot(T_f-T_m)$$

$$\frac{\varepsilon\cdot C_f}{P}\cdot\frac{\partial T_f}{\partial t}+\frac{v_0\cdot C_f}{L}\cdot\frac{\partial T_f}{\partial x}=h\cdot a_w\cdot(T_m-T_f)+q_{pr}+\frac{k_{eq}}{L^2}\cdot\frac{\partial^2 T_f}{\partial x^2}$$

The boundary conditions are assumed as perfectly insulated walls, and flat and constant temperatures T_c and T_h at the cold and hot inlets. The boundary conditions may be

modified to match a specific application setup, for example to model the effects of dead volume in flow plena, heat leak through the wall, etc.

The functions $C_f(T_f)$, $C_m(T_m,B)$, $D_m(Tm,B)$ are supplied to the model in tabulated form as properties of fluid and MCM. Specifically, the following properties of fluid are used: density ρ_f, isobaric heat capacity C_p, thermal conductivity k_f, and viscosity μ. The properties of MCM are supplied as heat capacity at zero field $C_m(T_m,0)$, adiabatic temperature change $\Delta T_{ad}(Tm,B)$ at a given field, and thermal conductivity k_m. The functions $C_m(T_m,0)$ and $\Delta T_{ad}(Tm,B)$ are converted inside the model into the entropy-temperature-field function $S_m(T_m,B)$ that is used afterwards to derive the functions $C_m(T_m,B)$ and $D_m(T_m,B)$:

$$C_m(T_m,B) = T_m \cdot \frac{\partial S_m(T_m,B)}{\partial T_m}; \qquad D_m(T_m,B) = -\frac{\partial S_m(T_m,B)}{\partial B_m} \cdot \left[\frac{\partial S_m(T_m,B)}{\partial T_m}\right]^{-1}$$

Parameters a_w, ε depend on the particular packing geometry.

The functions $h(v_0, a_w, \varepsilon)$, $q_{pr}(v_0, a_w, \varepsilon)$, $k_{eq}(v_0, a_w, \varepsilon)$ are defined via correlations for dimensionless Nusselt number, Fanning friction coefficient, and normalized equivalent conductivity $Nk = k_{eq}/k_f$ (or Peclet number), all three supplied as functions of Reynolds number and packing parameters. A number of packing geometry types are supported.

Functions and parameters $B(x,t)$, $v_0(t)$, L, P, T_c, T_h define particular design and operating conditions of the device. The supported profiles of magnetic field $B(x,t)$ include a trapezoidal field sliding over the bed from cold to hot end, in opposite, or sideways. The supported flow timing functions $v_0(t)$ include on/off flow switching and trapezoidal ramps.

The goal of the model is to solve the system of equations in respect to outlet temperatures of fluid for each direction of flow during the cycle. Solution is usually sought for the steady-state mode when each cycle repeats the previous one. Some characteristics of transient process may also be explored, such as bed cooling or heating pattern, time to steady-state, etc.

Based on outlet and inlet temperatures the cooling power Q_c and heat rejection Q_h are to be calculated as average net flux of fluid enthalpy, respectively at the bed's cold and hot end. Some other characteristics of the cycle can be deduced from Q_c and Q_h, such as work expenditures, coefficient of performance (COP), and efficiency in respect to Carnot cycle. Two additional supported figure of merits (FOM) were developed specifically for this program: Energy Efficiency Ratio (EER), and Seasonal Energy Efficiency Ratio for air-conditioning applications (SEER). To calculate the SEER, the model was run at five different temperature and load conditions that correspond to the full load and partial load test conditions used in calculating the SEER rating for an air conditioner. Additional FOMs available are the required mass or bulk volume of MCM, mass of magnet, or, for portable applications - total mass of MCM+magnet+battery supply for autonomous X-hours work. Any one of the FOMs can be chosen as an optimization parameter, the others – as rigidly specified or limited parameters.

The idea of the SA model is to solve the equations analytically, i.e. to find expressions for cooling power Q_c and heat rejection Q_h that involve only basic arithmetic, elementary algebra, simple interpolation, and standard functions provided by the underlying computer platform. As a result the calculations are fast (~0.1-1 seconds per run). This allows us to include the core model in various optimization loops or to use it to produce multi-point graphs of dependencies in the system.

SEP Optimization

The SA model was used in this program to do an optimization procedure for the SEP design in 2004-2005. The effort was preceded by a Finite Element Analysis (FEA)-based estimation of loss parameters (ffRe, Nu, Nk) for a number of regenerator matrices. The advanced geometry was considered as a general matrix geometry with the ability to vary the different dimensional parameters. Models were created for the first advanced regenerator geometry and the modified version of it, along with the second advanced regenerator geometry.

Each geometry was examined at two different flow rates to allow interpolation against Re. The interpolated formulae were plugged into the AMR SA model. The latter was used to optimize the SEP design for Gd MCM in terms of minimum bed volume for the given Qc and COP. The optimized parameters were flow rate, cycle frequency, internal regenerator dimensions, and bed dimensions (length, cross-section). Other parameters were fixed at limiting values (magnet field 1.5T, dwell ratio 1/3, etc.).

The first advanced regenerator geometry FEA could be done with a two-dimensional model, whereas the second advanced regenerator geometry FEA required a three dimensional model. Both could be modeled as a periodic series of identical unit cells. The loss parameters we are interested in are those typical of the developed flow in the matrix, rather than that in the entrance and exit regions. In order to approach the developed flow parameters, a model of a series of unit cells along the flow was constructed. The edges of the model parallel to the direction of the flow were chosen such that symmetry boundary conditions could be applied to minimize the required size of the model. At least three models were constructed for each geometry, one with N unit cells (typically N=3), the second with N+1, and the third with N+2. The difference in pressure drop and difference in heat transfer was computed between the N+1 and N cell models, and also between the N+2 and N+1 cell models. If the two sets of differences agreed within 0.5%, these differences were taken as the periodic cell heat transfer and pressure drop. Otherwise, a larger value of N was used until agreement within 0.5% was obtained.

In terms of sensitivity to manufacturing and assembly-induced tolerance, the first advanced regenerator geometry was inferior to the modified version. We thus had beds made from stainless steel in both of the geometries, and tested them as a passive regenerator, as discussed in the passive test section. The tests showed that as manufactured, the modified version had better performance than the first advanced regenerator geometry. However, the performance of both geometries were inferior to that predicted by the model for a mild geometric imperfection corresponding to that measured by a spot check of the components, indicating that either additional geometric variation came from assembly errors, or that multiple variations interact synergistically to reduce performance, an effect not included in the model. In addition, the observed pressure drop was slightly lower than that predicted

by the model, which was also consistent with the presence of certain kinds of geometric imperfections due to manufacturing and assembly errors.

We then had some test components of the modified configuration prepared in Gd by the same vendor that prepared the stainless steel components. Inspection of the components revealed extensive defects. The components were also much less rigid than the stainless steel components and thus harder to assemble. In light of the modeling and experimental results indicating the adverse effects of large amounts of geometric variation, we decided that this configuration for Gd was too high risk in the near term for the SEP. We also did not see a good long term solution for the technical problems of this configuration for useful MCM's.

We thus broadened the optimization process to look at another geometry, which is "analytical-friendly". A set of theoretical correlations was put together for all loss factors of interest: pressure drop, solid-fluid heat transfer, longitudinal conduction and dispersion. We used analytically-derived correlations for the idealized version of this geometry.

The SEP bed performance was then optimized with the SA model for this second advanced regenerator geometry in Gd. Optimized the geometric parameters led to a predicted specific cooling power of 1.7 watts per cc of bed, which is a bit better than that predicted for either the first advanced regenerator geometries.

The second advanced regenerator geometry is easier to fabricate in Gd than the first geometry, but it still has the risk of reduced performance due to manufacturing and assembly non-uniformities. The critical parameter in this geometry is not created in the MCM processing step, but there is still risk in the conventional material processing step. A test model comparing the results of two non-uniform beds in parallel flow to that of two uniform beds verified that the adverse effects of such non-uniformities can be significant, but we have not worked out a quantitative modeling technique for large scale random variations. We decided it was still worth building and testing a bed of Gd in the SEP because the key process variable is controlled by conventional processes in a conventional material.

Comparison of the test results of the SEP to the model results indicated, however, that good control of the regenerator geometry was not achieved in SEP, as is discussed further in the SEP testing conclusions section.

2.4.1 3TMAC modeling

We used the SA model to determine the size of components of a 3 ton magnetic air conditioner (3TMAC) in order to compare its cost to existing vapor cycle air conditioners. In contrast to the SEP, for the 3TMAC we calculated a projected performance based on use of future improved MCM's made in hydraulic diameters that we anticipate would be achievable with further development.

We used the second advanced regenerator geometry for modeling. The MCM is assumed to be a high performance $La(Fe_{0.88}Si_{0.12})_{13}H_y$ (LaFeSiH) series of materials that were studied in a parallel NIST ATP program. The LaFeSiH materials have a first order

magnetic phase transition that leads to a large magnetocaloric effect (MCE) and a large latent heat that acts like a large heat capacity at the Curie point. The Curie point of the LaFeSiH series can be adjusted from -80 to 55 C by adjusting the hydrogen content. Optimal performance would be obtained by using an AMR bed layered with a series of LaFeSiH materials of different Curie points arranged with the low Curie point materials at the cold end of the bed, and the high Curie point materials at the hot end of the bed.

The SA model assumes that the MCM used in the AMR bed has uniform properties throughout the bed, although these properties may be both temperature and magnetic field dependent. Thus the SA model is not set up to directly model a layered bed of LaFeSiH. However, because of the large latent heat of LaFeSiH, each layer of a layered LaFeSiH bed would stay at a nearly constant temperature equal to its Curie point during the AMR cycle, although the temperature of each layer would be different. Hence the behavior of a layered LaFeSiH bed would be approximately captured in the SA model by assuming a *uniform equivalent material* in the AMR bed that had a MCE as a function of temperature that was equal to the MCE of each LaFeSiH layer at its Curie temperature, and a heat capacity as a function of temperature that was equal to the heat capacity of each LaFeSiH layer at its Curie temperature. Optimal performance would be obtained if the layers and LaFeSiH compositions were arranged so the adiabatic temperature change was proportional to absolute temperature and the heat capacity were independent of temperature. We chose the adiabatic temperature change of the uniform equivalent material at the hot end of the bed to be that published for $La(Fe_{0.89}Si_{0.11})_{13}H_{1.3}$ in 2003, 6.9 K at 2T, or 3.45 K/ T. We also used an effective heat capacity of the uniform equivalent material of 1979 J/kg-K calculated from $Cp = T \times \Delta S/\Delta T$, where T was 291 K, the average temperature of the bed and the temperature at which ΔT was measured, ΔS that measured for the best LaFeSi material received from a vendor in 2005, 23.3 J/kg-K for a 0 to 1 T field change, and ΔT was the above value of 3.45 K/T. This manner of calculating heat capacity assumes that the magnetic latent heat of the material contributes to the effective specific heat. This uniform equivalent material should perform approximately as well as a LaFeSiH bed that might be made after further development, namely a properly layered bed made from LaFeSiH material with MCE equivalent to the best material made up to 2005.

Using the uniform equivalent LaFeSiH material in advanced regenerator geometry form, the SA model was used to minimize the required magnet mass of the 3TMAC over the range of bed parameters and magnetic field strength, with the restrictions that the net cooling power was 10.5 kW (3 tons of air conditioning) at design temperature span, and the EER was 12.5. This EER value led to a calculated SEER of 23. The bed and magnet size, the magnetic field strength, the fluid flow rate and pressure drop, and the drive speed, torque and power became inputs to the joint Astronautics-TIAX cost evaluation of the 3TMAC.

2.5 Synthesis and characterization of magnetocaloric materials.

The magnitude of magnetic entropy changes of $Gd_{1-x}Er_x$ materials with $x = 0.02$, 0.05 and 0.11 are about the same as that of pure Gd. Their Curie temperatures (and peak adiabatic temperature changes) are lowered by Er additions, and the concentration dependence is given by: T_c (in K) = $292.2 - 168x$. From three independent measurements of three

different spherical particles of $Gd_{0.93}Er_{0.07}$ it appears that the powder particles have consistent Curie temperatures. The magnetocaloric effect of spherical powders (magnetic entropy change) is only slightly lower when compared to that of bulk $Gd_{1-x}Er_x$ alloys prepared independently. Such small variations may be partly due to demagnetization effects, which were not corrected for. A plot of the magnetocaloric effect of one of the spherical particles is shown in Figure 2.14 below.

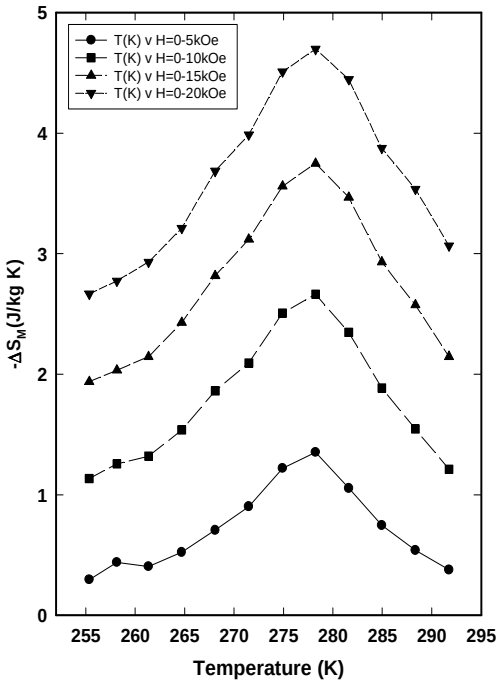

Figure 2.14: Magnetocaloric effect of a single spherical particle of $Gd_{0.93}Er_{0.07}$

The heat capacity C_p of $Gd_{0.89}Er_{0.11}$ (Curie point, $T_c \sim 271$ K and a C_p peak of ~ 52.1 J/mol K) and that of $Gd_{0.98}Er_{0.02}$ ($T_c \sim 287$ K and a C_p peak of ~ 57.6 J/mol K) display a λ-like behavior typical for a second order ferromagnetic-paramagnetic phase transition. It is worth noting that the T_c's obtained in heat capacity measurements are close to those obtained by measuring M(T) in a dc magnetic field, 274 K and 290 K, respectively.

The heat capacity of $Gd_{0.95}Er_{0.05}$ was also measured in several fields between 0 and 2.0 T dc magnetic fields (Figure 2.15 below). In a zero magnetic field, the observed T_c is ~ 283 K, which is about the same as that obtained previously from the magnetization measurements, and a C_p peak value of ~ 55.6 J/mol K. The typical λ-like peak is reduced in height and becomes rounded as the magnetic field is increased from 0 to 2.0 T, analogous to the heat capacity behavior of Gd metal near its Curie point.

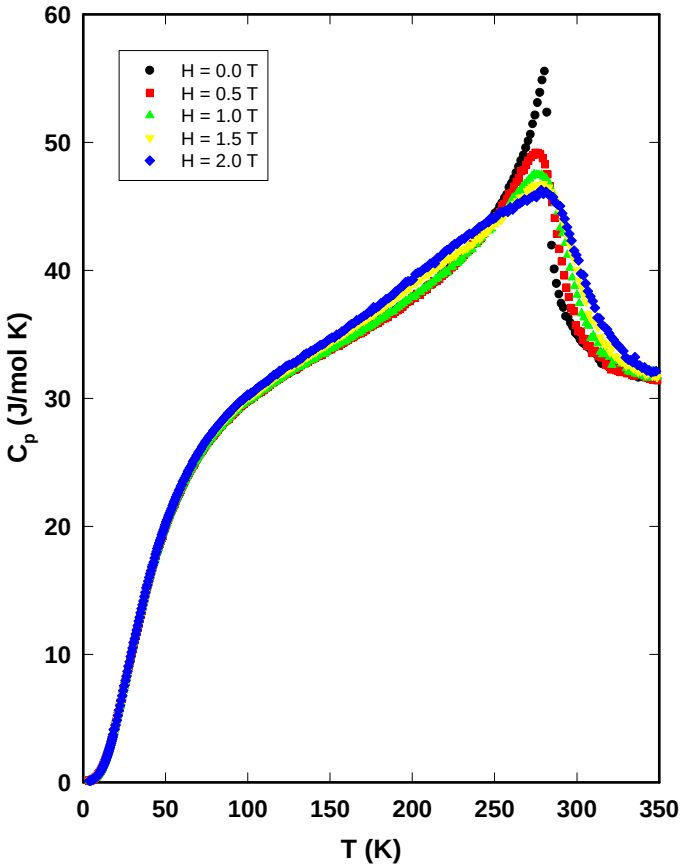

Figure 2.15: $Gd_{0.95}Er_{0.05}$ heat capacity measurement

The zero field heat capacity data, in conjunction with the magnetization measurements, allowed the entropy-temperature diagram, the adiabatic temperature change upon magnetization, and the isothermal entropy change upon magnetization to be calculated. The field dependent heat capacity measurements for the $Gd_{0.95}Er_{0.05}$ material allowed an independent check of the magnetocaloric effect calculations done using the magnetization data.

The magnetization of one of the Gd specimens selected from a batch prepared by one of the vendors for the SEP and the heat capacity for two specimens is shown in the two Figures 2.16 and 2.17 below. The heat capacities were essentially identical and had the expected values. Using the zero field heat capacity and magnetization, the magnetocaloric effect was calculated for a number of magnetic field values. The heat capacity and magnetization numerical data were also transmitted to Astronautics and were used as input data to the SA model to predict the performance of the SEP.

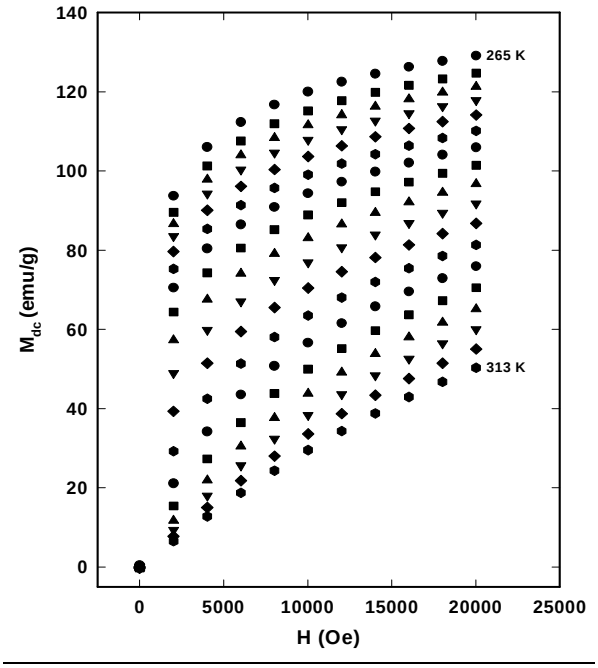

Figure 2.16: Magnetization isotherms of Gd prepared for SEP.

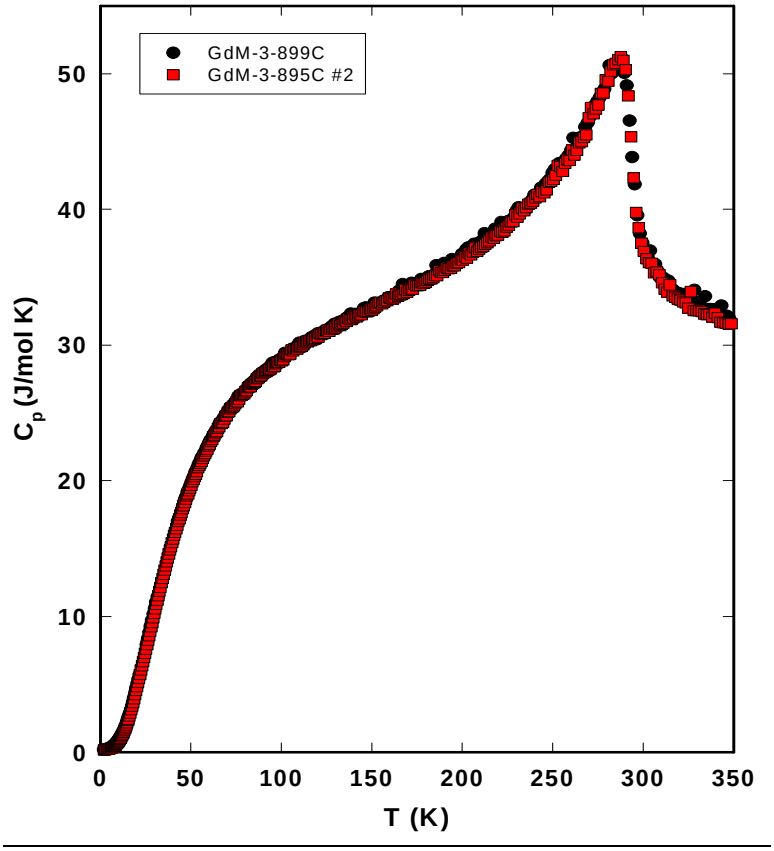

Figure 2.17: Heat capacity of Gd prepared for SEP measured in zero magnetic field.

The results of computing both ΔS and ΔT at the Curie temperature for Gd prepared for the SEP are summarized in Table 2.1 below.

Table 2.1: Maximum values of $|\Delta S|$ and ΔT obtained under different magnetic fields for the Gd (GdM-3-895C)

H (T)	-ΔS (J/kg K)	ΔT (K)
0.5	1.5	1.7
1.0	2.8	3.0
1.5	3.8	4.2
2.0	4.8	5.2

2.6 SEP design.

2.6.1 Selecting bed orientation and relative bed/magnet motion.

Based on preliminary AMR model results for the SEP, we examined various ways to arrange the magnetocaloric beds in a wheel and possible orientations for flow and magnetization. We considered tradeoffs involving magnet gap aspect ratio, valve design and location, plumbing layout, bed plenum design and other factors, when deciding whether to pursue a rotating magnet design or a rotating bed design. The number of beds and magnets also has an impact on the rotation decision.

We considered multiple options in parallel while the bed dimensions were still being optimized. For example, axial flow is appealing because two beds can be stacked end-to-end, sharing one plenum and isolating their cold ends from the surroundings. But if the bed length is too long, the magnet gap becomes too large, greatly increasing the magnet size.

Using the Gd material starting size and preliminary model output as a starting point, there were a limited number of options for utilizing the material. Taking into account the preferred aspect ratio for a magnet gap and our experience with building beds for the PRS, we designed bed modules around the resulting regenerator size. The bed modules were then incorporated into a wheel shaped structure.

We also designed a parameterized magnet assembly using FEA and went through several iterations of bed size and magnet design to find the best compromise between bed cross section and magnet gap cross section.

A comprehensive analysis of the engineering issues led us toward a rotating central magnet design with axial field and circumferential flow.

Additionally, a rotating magnet design allows much greater freedom in designing the valves, because the valves only need to control the flow switching. In a rotating bed design, the valves also need to transfer the fluid to the rotating bed assembly, and thus must be placed on the axis of rotation. In a rotating magnet design, the valves can be placed anywhere that is convenient, and any kind of valve design may be used.

2.6.2 Magnet design.

We started by designing and modeling a number of different magnet assemblies that can be adapted to different bed cross sections and radii. The magnet designs were analyzed with FEA for the various sets of bed dimension options. With feedback from the magnet analysis we narrowed down the range of possible bed cross section aspect ratios, and determined how much room is required within the bed wheel for the magnet, if the magnet were to have a flux return or other part of the magnetic circuit in the center of the wheel.

Within the bed wheel dimension constraints, it was challenging to achieve the required field strength over a long enough arc in the high field regions while preserving nearly zero field in the low field regions.

Information on one magnet assembly design was sent to one magnet vendor to solicit preliminary feedback on manufacturability. Discussions with representatives from another magnet company provided positive feedback. They said they would be able to produce both of the design options we discussed, and improved our understanding of the manufacturing process.

Magnet assemblies for three possible sets of bed wheel dimensions were been analyzed in detail. One of those combinations of bed width and height best provided the desired magnetic field, and the magnet design was refined around that geometry.

With the magnet assembly design finalized, we completed drawings and a written specification and requested quotes from a number of vendors. We carefully specified an envelope around the magnet assembly so the magnet vendor could add structural components as required while keeping clear of the regions around the magnet where we need access. Similarly, we specified a means to mount the magnet so we could continue designing the rest of the structure and drive system, but did not overly constrain the magnet assembly structural design which is the vendor's responsibility. Discussion with a visiting representative from another magnet vendor helped refine how to specify our intentions for the magnet assembly.

The two protrusions at each end of magnet assembly, shown in Figure 2.18, create the two high field regions that magnetize two portions of the ring of beds. Beds adjacent to the two curved parts of the assembly will be in the low-field regions. Each block of magnetic material in the picture has its own field direction.

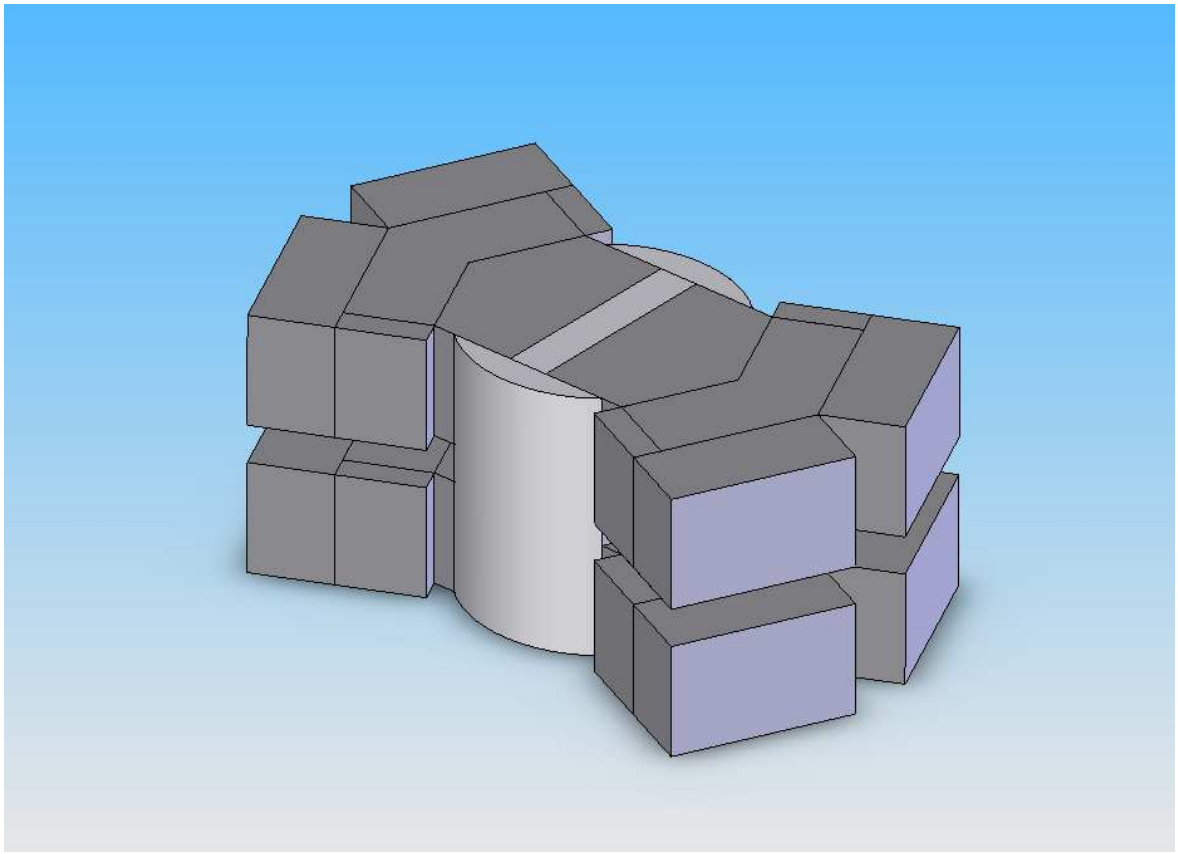

Figure 2.18: Solid model of SEP magnet assembly

A graphic output of our magnet assembly FEA is shown in Figure 2.19, in an orientation similar to the magnet assembly picture. The two low field and two high field regions of the magnet gap are shown, with contour plots on their surfaces illustrating the magnitude of magnetic field in Tesla.

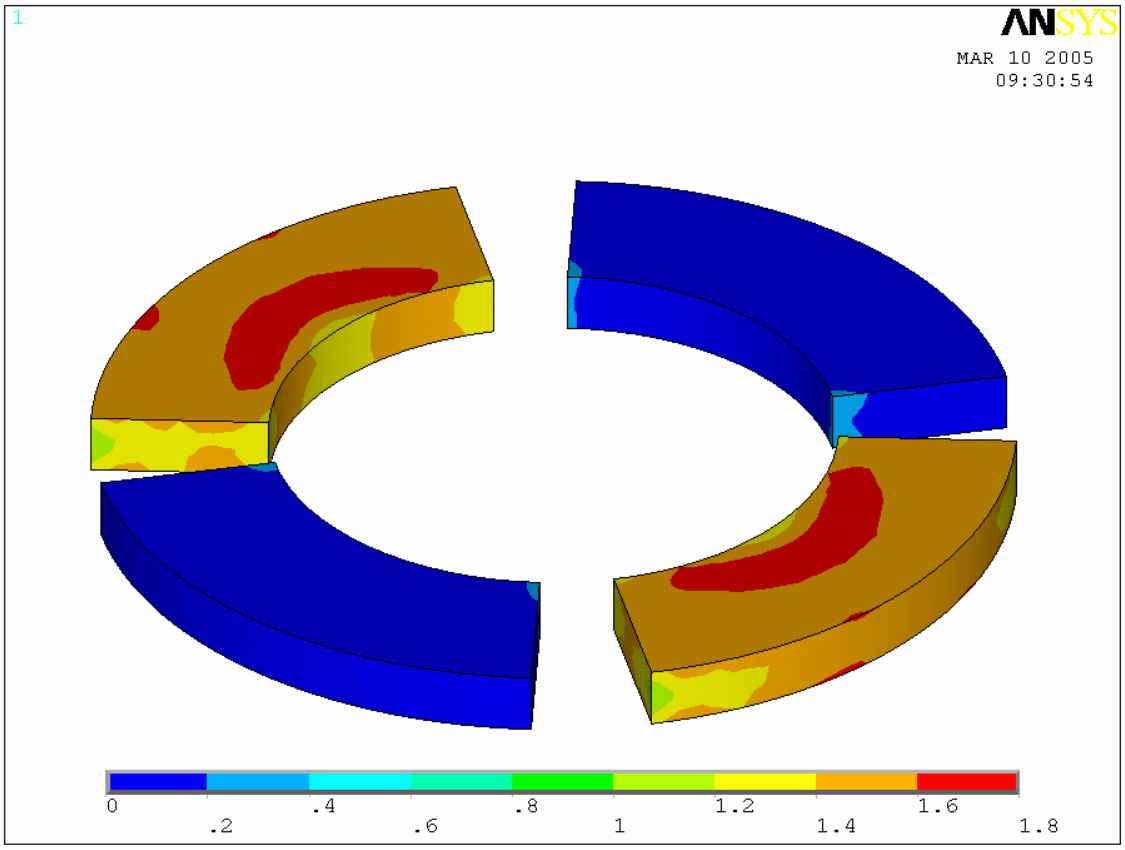

Figure 2.19: FEA results showing low and high magnetic field regions

We received six magnet assembly quotes and selected a vendor. The U.S. magnet company we selected had prior experience building Halbach array type magnetic assemblies and designing and building magnetic assemblies with high field uniformity requirements.

The magnet vendor provided an initial drawing of the structural support, and we worked out some issues regarding details of their design. The vendor has since provided an updated drawing, which we accepted as a basis for construction.

We designed a fixture to locate a Gauss meter probe in the air gap to measure the magnetic field at known physical locations. To measure the field in the magnet air gap, a Bell 640 analog gaussmeter was used in conjunction with the aluminum locating tool. A minimum of four readings were taken inside the gap at each angular increment, controlled by the locating tool. These measurement locations are depicted in Figure 2.20.

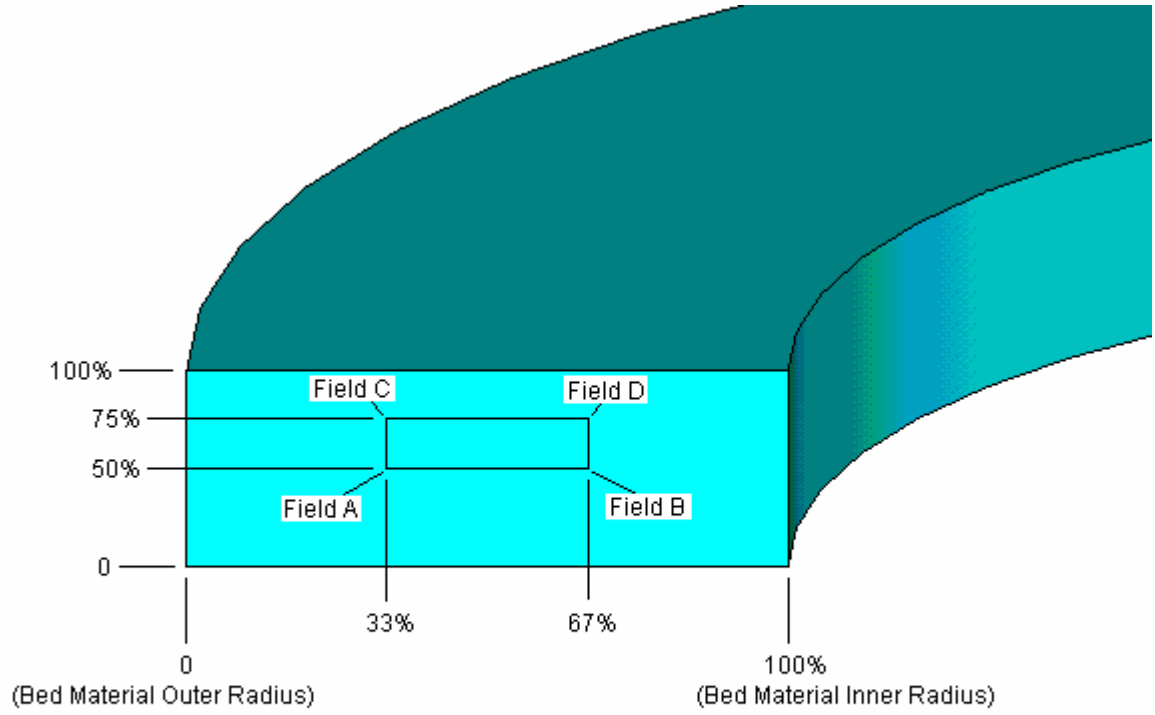

Figure 2.20: Field measurement locations.

For the first 180 degrees around the magnet assembly, measurements were taken at five degree increments. For the remaining half, this increment was increased to ten degrees after we established consistency between the two halves of the magnet assembly.

An FEA model of this magnet assembly, containing a small level of idealization, was modified to enable results tabulation at the same locations used for the physical measurements. These values were then compared to those taken with the gaussmeter.

The chart in the next figure (2.21) shows observed and modeled magnetic field at various positions in the gap as a function of angle around the magnet assembly. It is evident from the chart that the field gradients from the low to high field zones, as well as the entire low field zones themselves agree quite closely between the physical magnet and the simulation. In the high field zones there is some discrepancy with the physical magnet showing lower peak field values than the simulation by slightly more than 5%.

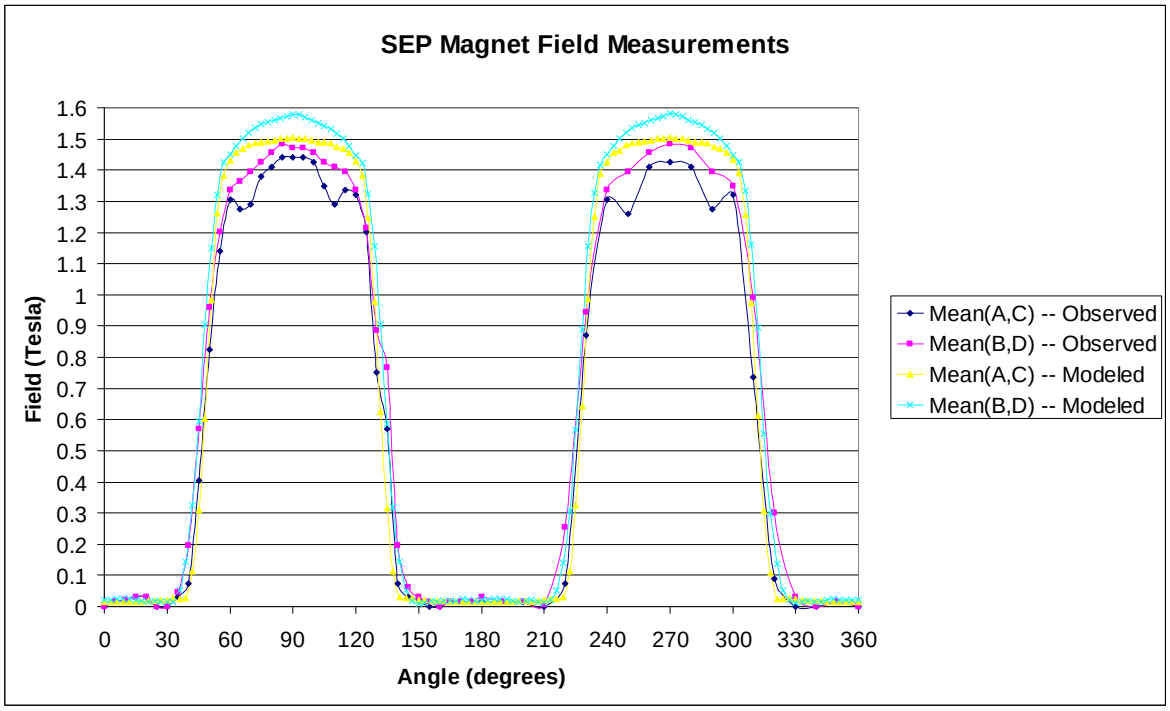

Figure 2.21: Observed and modeled magnetic field

The magnetic field is consistently shown to be slightly higher towards the inner bed radius (less than 5%) as predicted by the simulation.

The discrepancy between the peak fields is slight enough that it could conceivably be explained by a number of factors, including unaccounted for assembly means such as bolts and adhesives, a small error in the gaussmeter readings or simulation accuracy, or variance in the magnet material properties from the general specification.

2.6.3 Bed design.

2.6.3.1 Bed quantity and size.

We parameterized the Gd layout to most efficiently use the raw material. The size of the regenerator depends on the total cross sectional flow area required, the magnet gap aspect ratio that allows the most efficient magnet, and the physical limitations imposed by the size of the raw material.

Regenerator bed length was been added to the parameterized bed layout program so we could tradeoff bed cross sectional area and bed length and estimate the effect on cooling power. First the design was narrowed down to 12, 16, or 24 beds. The quantity 12 beds was finally selected based on model output for bed length and cross section, and magnet design iterations.

Partway through this process, after we finalized the magnet design, we changed the regenerator geometry from the first advanced regenerator geometry and instead used second advanced regenerator geometry. Since the magnet was already designed, the

number of beds, bed length and bed cross section were also fixed, so we had to work within those constraints while finalizing the bed geometry and physical structure.

2.6.3.2 Plenum design.

A good plenum design must achieve good flow distribution across the face of the bed and low pressure drop while having acceptable dead volume. After estimating the acceptable quantity of dead volume for the SEP, the bed plenum was extensively redesigned. The original plenum design exhibited low pressure drop and good flow distribution according to FEA fluid flow models, but the dead volume was unacceptably large. After conducting many CFD analysis iterations with various design features, we devised a plenum with acceptable dead volume that met our flow distribution and pressure drop goals. Additional analysis showed good flow distribution over a range of flow rates.

2.6.3.3 Structural design.

After designing the flow control portion of the plenum, we conducted a mechanical finite element analysis and modified the external part design to ensure adequate structural stiffness. The analysis was based on internal fluid pressure, estimated external magnetic force, and the bed mounting constraint. Bed deflection needs to be minimized due to the small gap between the magnet and the bed.

The bed structure is completely fabricated from G10 glass fiber-filled epoxy because of its combination of high strength and stiffness and low thermal conductivity. The bed structure gains much of its strength when both ends are bolted to thick G10 mounting plate that is stiff in compression.

The beds are cantilevered off of the mounting plate and exert significant magnetic bending force during AMR operation. After observing the bed mounting plate flexing slightly due to magnetic forces on the beds, we fabricated and installed stiffening posts to better support the plate. The stiffeners greatly reduce the flexing.

2.6.3.4 Thermal design.

In order to thermally isolate the hot end of the bed from the cold end, the only structure connecting the two ends of the bed are the four bed walls which consist of thin G10. The plenum at each end of the bed is combined with a mounting flange. The beds are mounted on a thick G10 plate. The mounting arms that bolt to the mounting plate are fairly long, both because the beds need to be cantilevered to reach into the magnet gap, and to limit thermal conduction along the mounting arm.

The beds themselves are not insulated, other than by the G10 structure, because the SEP is not designed to operate at temperatures low enough to cause condensation to be a problem.

2.6.3.5 Bed assembly.

The bed housing itself, consisting of the hot and cold plenums and bed walls, was designed to act as the assembly fixture for assembling the regenerator. This reduces the number of

assembly steps and ensures that the regenerator fits closely in the housing. This approach also reduces the number of individual part tolerances that must be accommodated in the assembly process. Integrating the construction of the housing and the regenerator improves the strength of the assembly as well.

The SEP bed structural design is nearly the same as the passive regenerator bed design used in PRS tests, except the PRS bed has one different plenum in order to interface with the PRS heater. During the PRS test we experienced leaks with the passive beds, which occurred at the joint between the end plate and the top plate, and caused concern that the SEP beds may have similar issues. Because the SEP beds fit closely in the magnet gap, there is not room for bulky external reinforcement. With this in mind we considered ways to improve the strength of the joints that do not require much space.

It is possible that the thin end plate bowed outward due to internal water pressure, causing the joint to develop a leak. To address this, we obtained thicker, substantially stiffer end plates. The thixotropic epoxy we use to seal the sides of the beds is also used to bond the side plate in place during the same step. This epoxy is not quite as strong as the epoxy we normally use, and by definition it does not flow as well, so we were careful to fully wet the joint with epoxy.

The SEP bed assembly process went more smoothly and quickly than expected. We were concerned about the beds leaking because of our experience with the similar PRS beds. On the bench we pressure tested the SEP beds with nitrogen, and discovered that they all had small leaks, similar to the PRS beds. It took three rounds of minor external repairs with epoxy, but we were able to fully stop the leaks. After repairs, the beds did not leak when pressurized to 50 psi with nitrogen.

2.6.4 Valve design.

The rotary disk valves for the SEP were initially developed under a parallel program. We completed valve development and implemented the valves under this program.

The valve utilizes one rotating and one stationary ceramic disk to provide a low friction seal and to switch flow from one inlet to six outlet ports, or in some cases from six inlets to one outlet port. A small stainless steel shaft drives the rotating disk. A standard shaft seal on this shaft is the only dynamic seal needed to prevent external leakage.

Feedback from the ceramic component vendor guided our design for the ceramic disks regarding feature shape and tolerance, and we used CFD software to minimize pressure drop inside the valve. The diameter of the valve disk is a tradeoff between a large port diameter that reduces pressure drop, and a small disk diameter that reduces sliding friction.

Four separate valves are needed to control flow to and from the 12 AMR beds: hot inlet valve, hot outlet valve, cold inlet valve, and cold outlet valve. All four valves are the same, only differing in their relative phase. We purchased two sets of rotor disks that provide two different dwell ratio options.

2.6.5 Drive system design.

The magnet and valves are driven by a variable speed, permanent magnet, brushless DC motor and gearbox using a system of timing belts.

The bearings for the magnet shaft have non-magnetic balls and retainers. If the balls or retainer in the bearings that support the rotating magnet are attracted to the magnet they will prevent the bearings from turning freely and increase friction and wear. Even though the bearings are located in regions where the field is low, to eliminate the possibility of magnet field-induced friction, we chose bearings with ceramic balls and Teflon retainers.

A unique aspect of the drive system is the torque measurement flexibility. The system of shafts and pulleys allows for three belts configurations to measure the magnet drive torque, the valve drive torque, or the total torque provided by the motor, using a single torque meter.

2.6.6 Fluid system.

The SEP fluid system can be divided into two sections, the parts of the system that control and distribute fluid to and from the beds, and the parts of the system that provide fluid flow and the heat load and heat sink. The flow control and distribution system consists of the four rotary disk valves discussed in the valve section and the network of tubes connecting those valves to the beds. Each valve has one common port and six inlet or outlet ports. Each inlet or outlet port splits into two tubes that connect to opposite beds. Each bed has four ports, hot inlet, hot outlet, cold inlet and cold outlet, which connect to the corresponding valve. This network of 48 tubes is physically divided into two sections, with the hot inlet and outlet tubes and valves located above the plane of the beds, and the cold inlet and outlet tubes and valves located below the plane of the beds.

The rotating SEP magnet could act as a fan, promoting forced convection heat transfer into the cold plumbing. Calculations show that the moving air increases the heat transfer by a factor of four. To prevent this the cold tubes are isolated from ambient air and the moving air caused by the rotating magnet by enclosing them in a donut shaped region consisting of parts of the SEP structure above and below, and plastic walls at the inner and outer diameter. The hot tubes are not isolated from ambient because their temperature is at or above room temperature, and rejecting heat to ambient is not detrimental to device performance.

To improve overall performance as well as experiment repeatability we insulated the cold tubes going to and from the cold heat exchanger. We also insulated the hot inlet tube that connects the hot heat sink to the hot inlet valve in order to improve experimental control.

The SEP pump is a DC motor-driven diaphragm pump. The pump is not sized for optimum efficiency at a particular operating point, but does provide enough flexibility to operate over a wide range of pressure and flow rate conditions.

The heat load for the SEP is an electric heating element with adjustable output, adapted from components of a commercially available tankless water heater. The main

requirement for the heater system is an energy balance one: essentially all the electrical power supplied to the heater must enter the fluid stream, rather than escaping into the environment. This is important because the heat load is calculated from electrical voltage and current measurements. Measuring electrical power input is more accurate than calculating power from fluid flow rate and entering and exiting fluid temperatures because the temperature difference across the heater (around 1 degree C) is too small to measure accurately. The energy balance requirement means the heater must have good heat transfer between the heater and the fluid in order to reduce the temperature the heater must reach in order to transfer enough heat, thus reducing heat leaks to ambient. The heater system is also well insulated to prevent external heat leaks. Additionally, the heater system should have low pressure drop to minimize the parasitic load on the fluid pump, which reduces calculated overall efficiency.

2.6.7 Instrumentation.

The SEP can be configured to measure the total input torque or the valve input torque or the magnet input torque, all by switching belt locations. The torque meter for the SEP is a high precision, in-line type that can respond quickly to varying torque. We specified the full scale range to be somewhat larger than the predicted maximum average torque because of uncertainty in our AMR cycle modeling, peak torque loads that may be significantly higher than the average, and increases in torque at the largest temperature spans.

The flow meters must be placed far enough from the magnet assembly to prevent magnetic interference. Because the flow meter vendor does not have a specification for magnetic field tolerance, we conducted a test to verify the absence of interference.

The data acquisition system mainframe hardware is a flexible system that is mostly used to make precise steady-state measurements, but it is also capable of recording high-speed data for diagnostic purposes.

The data acquisition system is based on the National Instruments SCXI series of digital components. The system for the SEP includes a control module, two 32-channel thermocouple-compatible input modules, a 32-channel current excitation module, and the necessary chassis, terminal blocks, and cables. This system communicates via USB with a PC running LabVIEW software. The National Instruments hardware calibration is NIST-traceable.

The water temperature at the hot outlet of each bed and at the common leg of each valve is measured with YSI 44000 series precision temperature sensors in sealed stainless steel tubular probes. The temperature sensors are interchangeable to +/- 0.1 º C, and their calibration is NIST-traceable.

Flow Technology FT series turbine flow meters are used to measure the water flow rate on the hot and cold sides of the flow circuit. The flow meter calibration accuracy is +/- 0.05% and is traceable to NIST. The flow meters we are using have the optional 30 point water extended range calibration. We are also using Flow Technology Linear Link linearizing electronics, specifically calibrated to each flow meter, to provide linearized output to +/- 0.1% of the reading over the entire range of the flow meter.

The water pressure is measured at the common leg of each of the four valves. Setra model 206 capacitive sensor pressure transducers provide +/- 0.13% of full scale accuracy, and their calibration is NIST-traceable.

A US Digital optical encoder and two US Digital digital-to-analog converters measure the position and rotation speed of the magnet.

All of the hardware and sensors mentioned above are new and have been selected and purchased specifically for this program.

2.7 SEP test results.

2.7.1 Bed pressure drop.

Before final assembly of the SEP, each of the SEP beds was individually installed in the PRS apparatus in order to measure its pressure drop. The following Figure 2.22 shows the pressure drop for each bed with constant flow at 2.5 LPM. The variation in flow impedance between the beds is greater than desired. When two beds are undergoing flow in parallel in the SEP, unequal impedance causes unequal flow rates in the beds. Unequal flow hurts performance because lower flow impedance is correlated with lower heat transfer between fluid and solid. Thus the low impedance beds take the most flow but are the least effective at transferring heat to the fluid.

The pressure drop measurements also showed that the Gd SEP beds have much higher flow impedance than the stainless steel PRS beds, which are nominally the same design. For a give flow rate the SEP bed pressure drop is approximately twice as large as the PRS bed pressure drop.

The high flow impedance and the variation in flow impedance indicate that the beds do not have the precise, consistent internal geometry required for a highly effective regenerator.

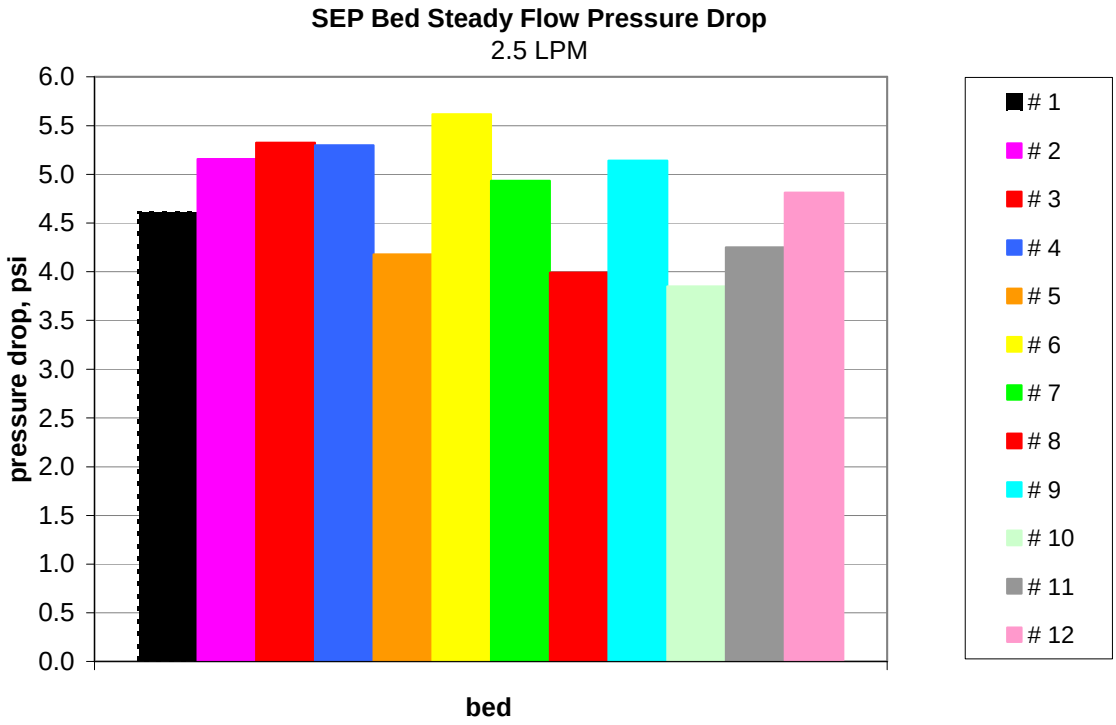

Figure 2.22: SEP bed pressure drop measurement

2.7.2 Load testing.

The SEP began cooling down immediately when it was first turned on. The device is responsive in the expected manner, with cooling power generally increasing with increasing flow rate, and larger temperature spans achieved when operating close to gadolinium's Curie temperature.

A series of load tests, where for a given flow rate and frequency the heat load is varied from the maximum heat load (producing zero temperature span), to zero heat load (producing the maximum temperature span) illustrate the current SEP performance. We conducted load tests for three rotation speeds, three flow rates, and two hot inlet temperatures.

The next figure (2.23) shows the results from the 24 C hot inlet temperature load tests. Tests were conducted at 60, 90, and 120 RPM, and 1, 2, and 3 LPM. The results clearly show maximum cooling power increasing with flow rate as expected, because cooling power at low span is essentially the product of the temperature change due to the magnetocaloric effect and the flow rate. The no-load temperature span increases when the flow rate is increased from 1 to 2 LPM, but does not increase much with the increase in flow rate from 2 to 3 LPM.

At the highest flow rate, 3 LPM, the maximum temperature span and the maximum cooling power increase with the rotation speed, with 120 RPM resulting in more cooling power and a larger temperature span than 60 or 90 RPM. At 1 LPM, however, the

maximum temperature span and the maximum cooling power at 120 RPM are lower than that at 60 and 90 RPM. As the rotation rate is increased, the heat transfer losses in the magnetization/demagnetization part of the cycle increase, but the utilization ratio in the flow part of the cycle decreases, leading to lower regeneration losses. It appears that at 3 LPM, regenerator losses dominate, leading to best performance at 120 RPM, while at 1 LPM, the smaller utilization ratio has a smaller effect than the magnetization losses, leading to best performance at 60 RPM.

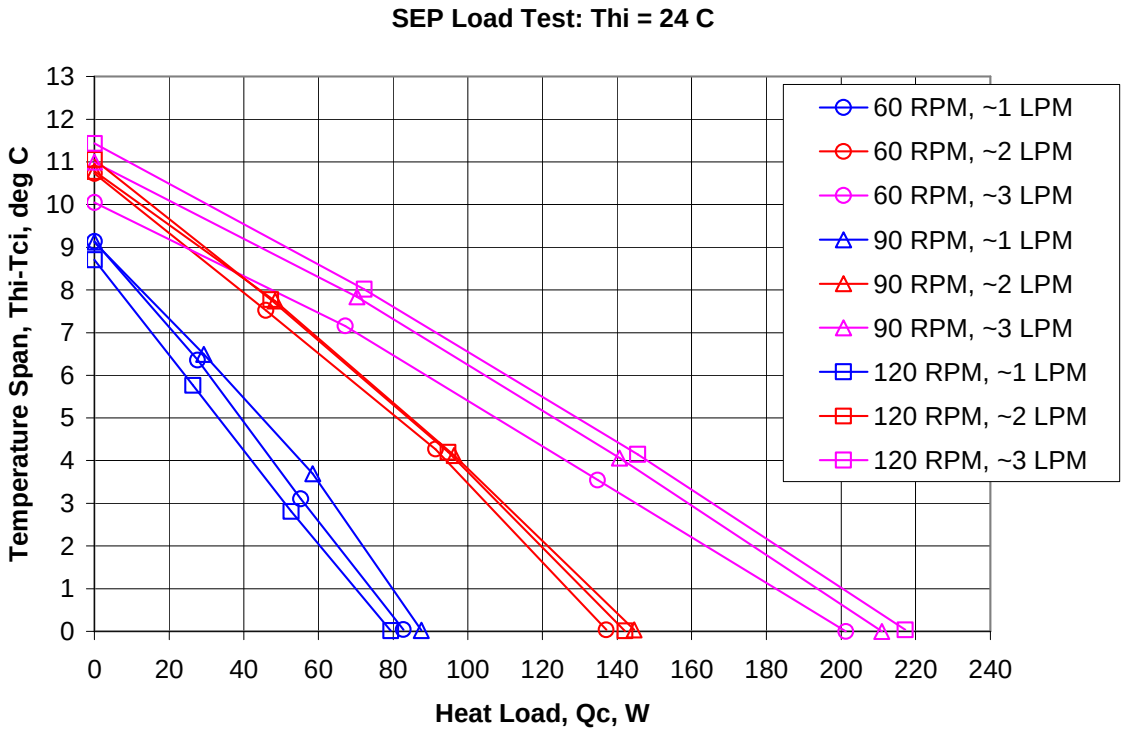

Figure 2.23: SEP load tests with 24 C hot inlet temperature

Figure 2.24 shows results for the same series of tests conducted with the hot inlet temperature set to 36 C. The overall performance is lower because the beds are operating farther from the Curie temperature of gadolinium, so the magnetocaloric effect is smaller.

The maximum cooling power again increases with flow rate, but this time there is more dependence on rotation speed. This may be the result of increased dependence on utilization ratio at this temperature, because the heat capacity and magnetocaloric effect of Gd decreases above the Curie point. Since most of the bed is above the Curie temperature and only part of the bed is participating in the active magnetic regenerator cycle, the bed is more sensitive to excessive flow.

At zero load the situation is different from the 24 C case. With the 36 C hot inlet temperature, the temperature span is larger for the lower flow rate points.

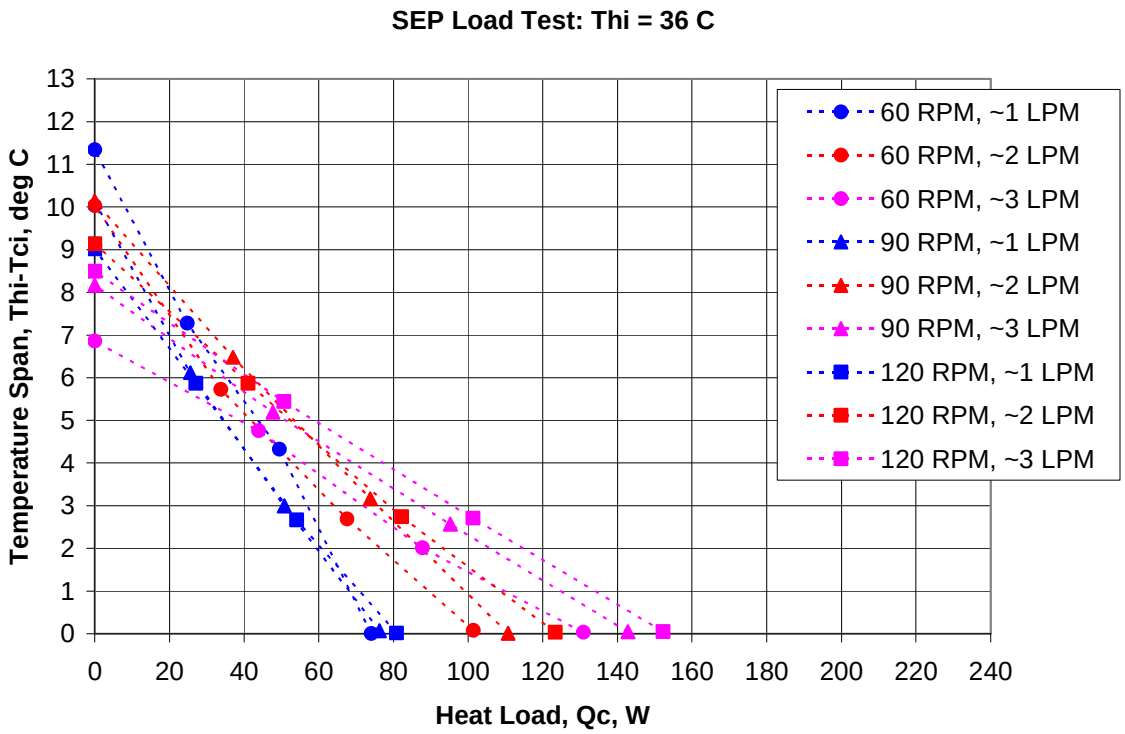

Figure 2.24: SEP load tests with 36 C hot inlet temperature

2.7.3 Efficiency.

The efficiency of the SEP can be calculated from the data recorded in the load tests. The coefficient of performance, or COP, can be calculated two ways. In all cases the cooling power is the product of the electrical current and voltage in the heating element. Cooling power could also be calculated based on fluid flow rate and entering and leaving temperatures, but because the temperature difference is so small the temperature sensors are not accurate enough for that approach. The electrical COP is the ratio of cooling power to electrical power input. The pump and drive motor electrical input power are calculated from their respective voltage and current.

The COP can also be calculated on a work basis, using the flow and shaft input work. The flow work is calculated based on the average flow rate and system pressure, including the valves and beds and cold heat exchanger, but not including the filter and hot heat exchanger. The shaft work is calculated from the rotation rate and the motor output torque. The measured torque includes the torque required to rotate the magnet, the valves, and the rest of the drive train shafts and belts and pulleys.

The next figure (2.25) shows the work input-based COP for the SEP when operating with the hot inlet temperature at 24 C. In general, the efficiency increases as the heat load increases. This is because as the heat load increases the temperature span decreases, reducing the net magnetic force on the drive.

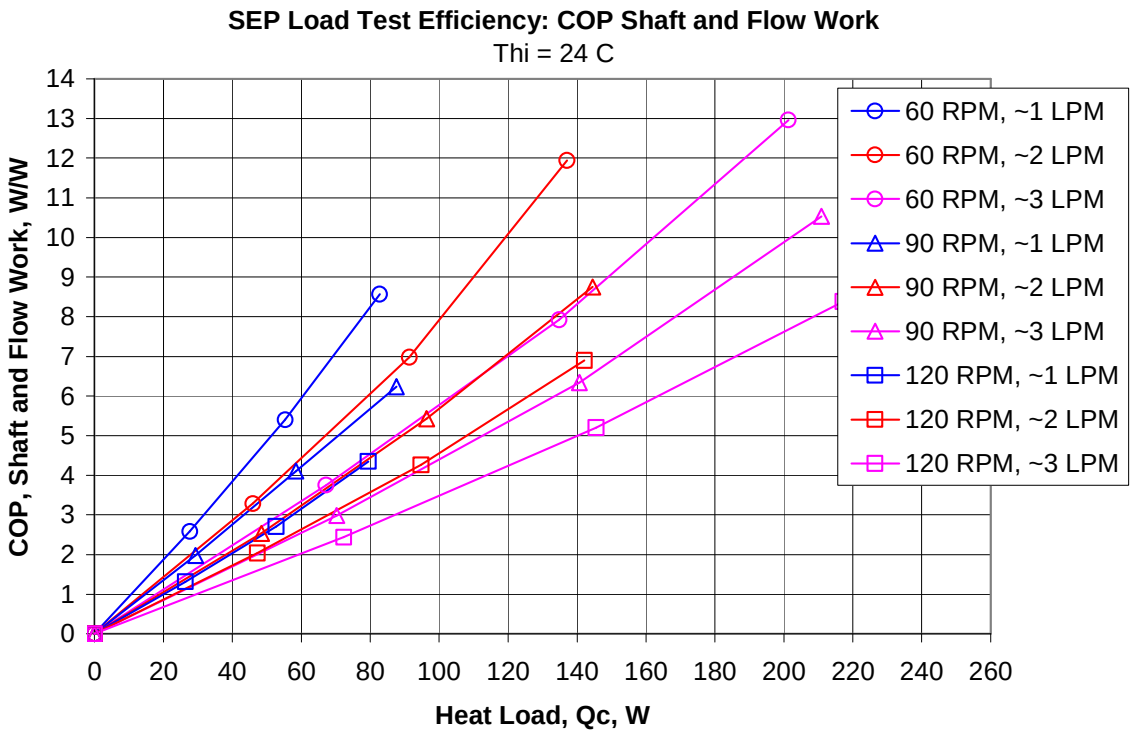

Figure 2.25: SEP work input COP for Thi = 24 C

The next figure (2.26) shows the work input COP for the 36 C hot inlet temperature load tests. The curves have similar slopes, but do not reach as high efficiency as the 24 C tests because the maximum heat load is lower for the 36 C tests.

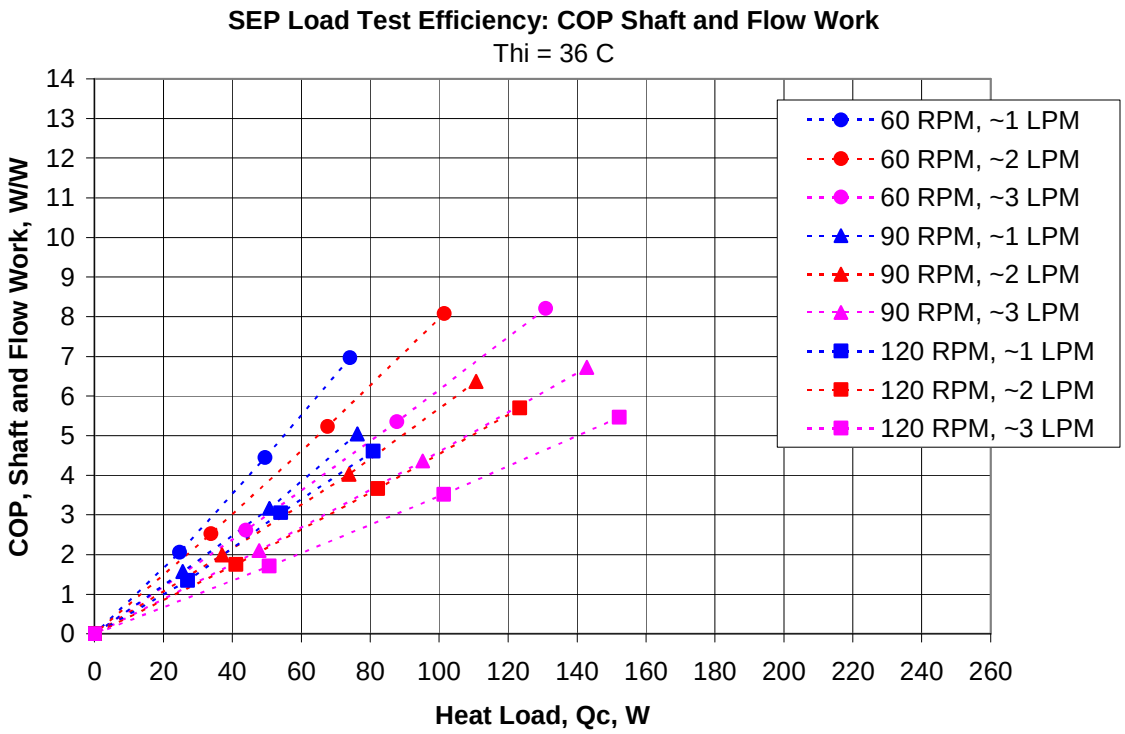

Figure 2.26: SEP work input COP for Thi = 36 C

The COP calculated using electrical input instead of work input is much lower, as shown in Figure 2.27 for the 24 C load tests. Calculating the efficiency this way includes the inefficiency of the drive motor controller, the electric drive motor, the drive motor gearbox, the electric pump motor, and the pump itself. Typical drive and pump electrical operating efficiencies during these tests were 25% and 18%, respectively. The SEP electrical efficiency could be substantially improved by specifying a drive and pump that are optimized for the SEP operating regime. The SEP drive and pump were sized for the original design specification, which called for higher torque, higher flow rate and lower pressure.

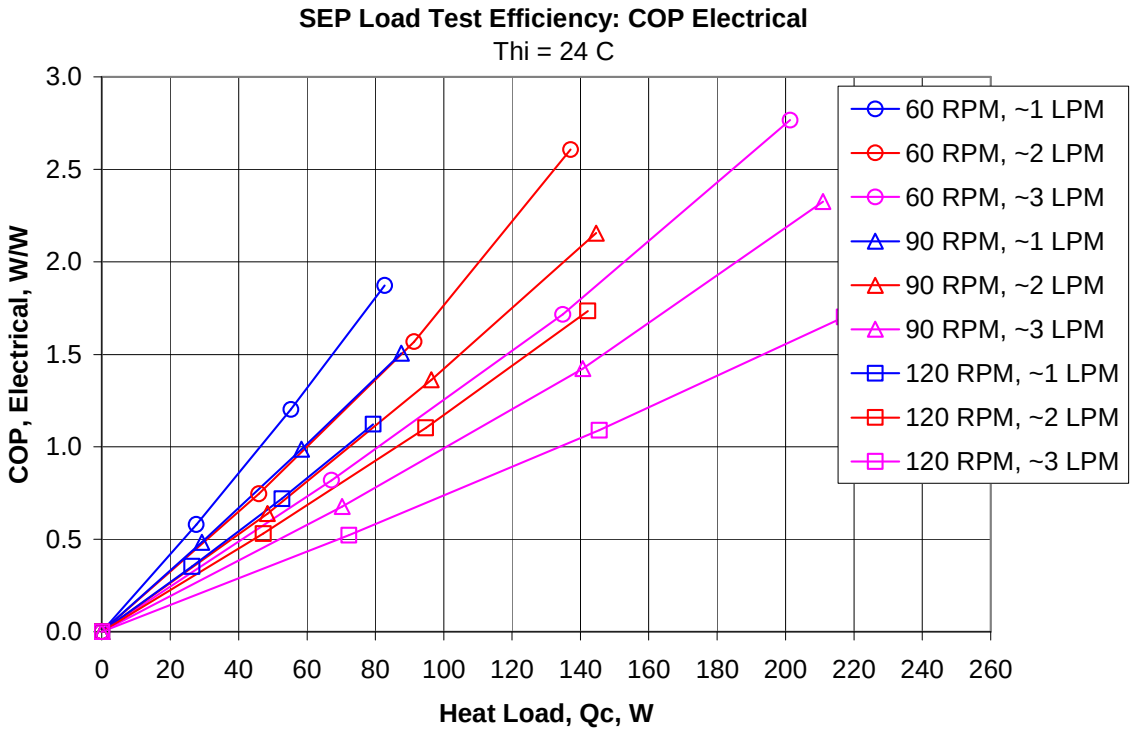

Figure 2.27: SEP Electrical COP for Thi = 24 C

The next figure (2.28) shows electrical COP for the 36 C hot inlet temperature load tests. The curves are similar to the 24 C curves, but again the SEP did not achieve as large cooling power at this higher operating temperature.

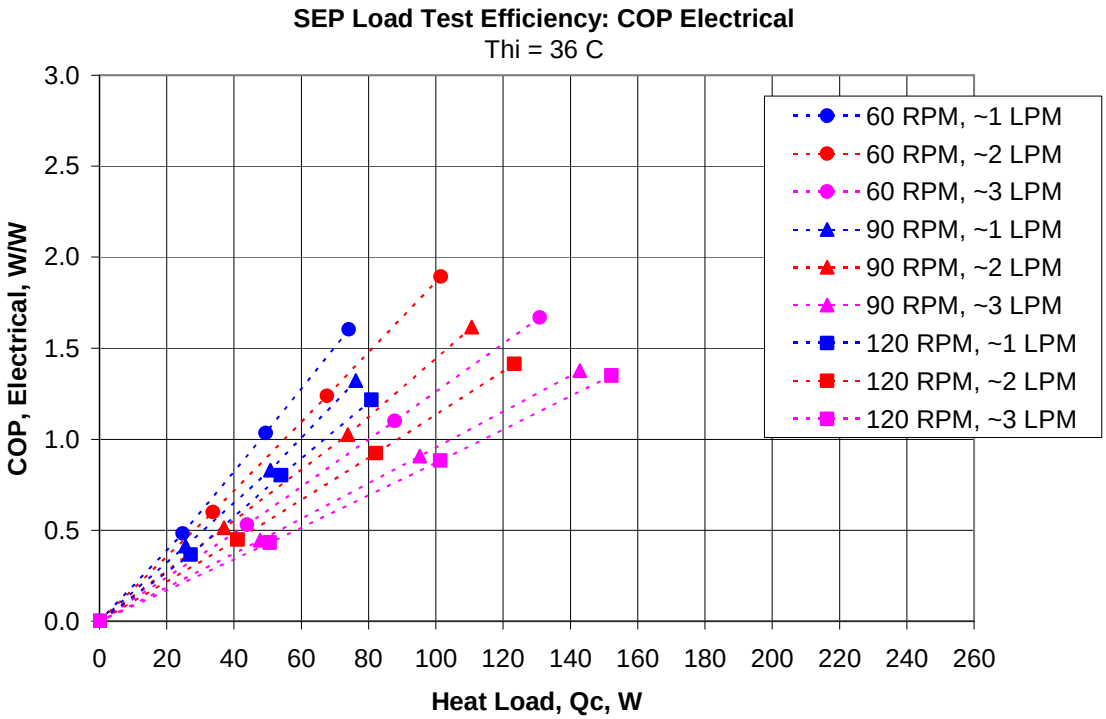

Figure 2.28: SEP Electrical COP for Thi = 36 C

2.8 Magnetic Air Conditioning cost analysis.

2.8.1 MAC modeling.

Using our AMR modeling, design, and magnet modeling tools and experience, Astronautics produced initial and revised specifications for a high efficiency 3 ton magnetic air conditioner (MAC). These specifications were used by TIAX to estimate the cost of producing the MAC in quantity. We also produced a specification for a reduced cost and efficiency 3 ton MAC. The specification includes water flow rate and pressure drop, entering and leaving water temperatures, drive motor shaft speed and torque, bed size, and magnet size and mass.

Integrating the seasonal energy efficiency ratio (SEER) calculation into our thermodynamic optimization model ensured that the device is optimized for the full range of operating loads and temperatures. Operating at SEER conditions is an advantage for magnetic refrigeration systems, which tend to operate at improved efficiency under partial-load conditions, as opposed to conventional vapor compression systems that operate less efficiently at partial load. Conversely, we have also included more realistic external losses, including heat leaks and fan power, which reduce the overall system efficiency. The model can now accommodate variable speed heat exchanger fans so that at low load conditions the fans do not require full input power, which substantially impacts system efficiency at points where magnetic refrigeration illustrates its improved efficiency.

In modeling the 3 ton MAC, it became apparent that meeting the SEER efficiency was not the main challenge. External losses make it difficult to achieve high efficiency under full

load (EER) conditions while maintaining modest bed size and magnetic field strength. External losses include heat exchanger and plumbing pressure drop, heat leaks, drive motor and pump inefficiency, and heat exchanger fan power. When we picked a minimum EER, the resulting SEER always exceeded our target.

2.8.2 MAC costing.

TIAX performed three major functions in supporting the magnetic air conditioner (MAC) development project.

- Optimum sizing of "balance of system" – indoor and outdoor coil assemblies and interconnecting lines – to match cost-effectively the operating temperatures, water flow, and cooling capacity and heat rejection of the MAC chiller unit, while limiting air and water moving parasitics to levels consistent with system performance goals.
- Manufacturing cost analysis of the complete MAC system and comparison with a high-SEER vapor cycle air conditioning system.
    - Following a manufacturing cost analysis methodology.
    - Using relevant manufacturing cost data developed to support DOE residential and commercial air conditioner efficiency standard setting rulemakings.
- General input on air conditioner system issues – e.g. variable capacity SEER test procedure, indoor coil temperature for adequate dehumidification, basic market data for cooling equipment categories to which the MAC is applicable.

Summary of MAC Manufacturing Cost Stacks

Manufacturing costs were estimated for several versions of the MAC and, for comparison, for typical vapor compression cycle central air conditioning systems at two SEER levels (13 and 18). Previous manufacturing cost analysis in support of a recent NAECA energy efficiency standard setting rulemaking provided cost models and component cost data for conventional vapor cycles and for the conventional components – coils, fans, blowers, sheet metal – that are used in the MAC.

<u>High SEER Configuration</u>

The direct manufacturing cost of the high-SEER Magnetic Air Conditioner (MAC) was compared to a conventional high SEER vapor compression (VC) cycle. All components of the complete system are included for both. The reduction in cost from the first iteration of the high-SEER configuration is the result of:

- Adjustments in coil sizing in response to changes in the entering and leaving water temperatures and flow rates of the MAC chiller, resulting in a modest increase in the outdoor coil face area and a decrease in the number of rows of tubing in the indoor coil.
- Lower cost NeFeB magnet material was identified.

The Direct Manufacturing Cost for the 18 SEER VC system was found to be $865 and the 23 SEER MAC system was found to be $1188.

Low-Cost MAC Configuration

The low-cost version of the MAC trades some efficiency (SEER) for reduced cost. The changes in the system design:

- Replace ECM motor for indoor blower with a constant speed induction motor
- Reduced NeFeB magnet weight
- MCM beds reconfigured, results in reduced flow rate but more pressure drop, net effect is pump motor is increased from ¾ to 1 horsepower
- Indoor and outdoor coil operating temperatures and flows are essentially unchanged, so coil designs are unchanged from the 23 SEER configuration

The direct manufacturing cost of 13 SEER VC system, 18 SEER VC System, and 13 SEER MAC system was found to be $749, $865, and $1065, respectively.

2.8.3 Coil Sizing and Cost Estimates.

For each magnetic air conditioner configuration, TIAX sized indoor and outdoor coils:

- To cost effectively provide the cooling and heat rejection capacities required at the specified chilled water (for cooling) and warm water (for heat rejection) temperatures and flow rates
- To minimize parasitic power – water pumping and air moving – subject to cost effectiveness

2.8.4 Alternative Heat Exchangers.

The MAC system operates at low (20 psi maximum) water pressure. Several alternate coil configurations were identified as having the potential to take advantage of the low water pressures of the MAC system, providing lower costs:

- All plastic coil
- Automotive radiator configuration
- Microchannel/other aluminum extrusion

While each alternative remains a promising alternative for reducing coil cost, we were unable to obtain definitive cost information.

2.8.5 Freeze protection.

The 3 ton MAC was designed to use water as a heat transfer fluid. A comprehensive analysis indicated that freeze protection can be provided with a modest impact on MAC system design. Main factors to consider are:

- The results for fixed coil designs (which were optimized for 100% water) show that adding 30% methanol causes a capacity drop at the same volume flow rate. Increasing the volume flow rate can restore the capacity, but with an increase in pumping power.
- A better adjustment is to make a modest increase in coil size, coupled with smaller adjustments in flow rate, so that the overall impact on coil size and performance is modest.
- In the magnetocaloric beds, the impact of water-methanol mixture properties would also need to be considered.
    - Lower mixture specific heat and density.
    - Lower mixture thermal conductivity.
    - Interaction between methanol in aqueous solution and the magneto-caloric material.
- While water/salt solutions nominally have transport properties closer to water, the disadvantages may outweigh the heat transfer performance advantage, due to potential compatibility/corrosion issues with salt solutions. These issues will be examined in future projects.

2.8.6 Comparison of Heat Transfer Performance of Coils with Water and With Refrigerant.

The size and cost of the outdoor and indoor coils for the MAC have been compared with the size and cost of the condenser and evaporator coils used in high (18) SEER vapor cycle air conditioners. A comparison of vapor cycle and water heat exchangers indicate that the overall cost for equivalently sized refrigerant and water coils could be roughly the same in optimized systems.

2.8.7 Manufacturing cost analysis.

Manufacturing costs were estimated for several versions of the MAC and, for comparison, for typical vapor compression cycle central air conditioning systems at two SEER levels (13 and 18). Previous manufacturing cost analysis in support of a recent NAECA energy efficiency standard setting rulemaking was the basis for much of this analysis.

<u>Costs of Major Components and Materials of the MAC Chiller Assembly</u>

Assumptions for the cost analysis of parts and components unique to the MAC Chiller Unit:

- Volumes of 75k per year
- 2 year life cycle on mold design
- Purchased parts delivered monthly in lots of 6250
- Manufactured part costs determined through an auto industry oriented software package. (Piece part prices were scaled – *increased* – due to lower volumes)

Magnet Assembly
The magnet assembly is a "C" configuration magnet consisting of two high energy (NdFeB) permanent magnets and an iron core that completes the magnet circuit. Cost estimates were made for a cast and finish machined iron core for the magnet assembly. Magnet cost modeling was based on dimensions provided by Astronautics.

We have had discussions with 5 vendors regarding Grade 48 NdFeB magnet pricing. Vendors were given the option of making the large magnet arc for the MAC unit in one or several segments. Based on vendor feedback, it would be manufactured in 3-4 segments and bonded to create the arc.

In response to these inquiries, high-volume price quotes were received from 5 suppliers ranging from $331-$456 per pair.

Drive Motor
Two design options for the 2.5 HP, 900 RPM drive motor were investigated. The first of these options is probably the better of two, because a standard, readily available motor is used, and the estimated cost is somewhat lower.

- 2.5 HP, 1750 RPM 4 pole drive motor
  - Common in HVAC applications
  - V-belt and 2:1 pulley step down assembly required to drive the rotating AMR bed assembly at 900RPM

- 2.5 HP, 900 RPM 6 pole open frame drive motor
  - Custom design

Rotary Valves
An initial cost model for the rotary valve has been developed based on an Astronautics design. Each disc will be pressed from graphite and requires secondary machining for the face and holes.

2.8.8 Component Specification and Parasitic Power.

Parasitic power is the (electrical) power required to circulate the air and coolant flows needed to transfer heat in and out of and within the MAC.

The indoor and outdoor coils were designed to meet the required heat transfer, with the allocated parasitic power, while keeping the cost of these coils competitive with vapor cycle. The parasitic power depends on the ideal hydraulic power (flow rate times pressure drop) required to force the air and water flows through the coils and the MAC chiller unit and the efficiency of the motors, fans, blowers, and pumps that actually drive these flows.

2.8.9 SEER calculation for a residential central air conditioning system with capacity modulation.

An advantageous characteristic of the AMR chiller is that the cooling capacity can be continuously modulated efficiently over a 3 or 4 to 1 turndown range by varying the water flow rate, similar to the continuous capacity modulation provided by a variable speed compressor in a conventional vapor cycle air conditioner. Capacity modulation generally increases the SEER by 30% to 40%, compared to on-off capacity control, by eliminating on-off cycle losses, utilizing heat transfer surface more effectively and reducing average blower power. The DOE energy test procedure for residential central air conditioners, (10 CFR Part 430, Subpart B, Appendix M) includes a variable speed test and SEER calculation procedure. The key parts are Section 5.1.6, the bin hour chart in Section 6.1.2, and Section 5.1.3 (which is referred to for Case III). Also Section 3.1.6 spells out the required test points. The SEER is determined by a bin analysis (Table 2.2), where the individual bin cooling capacity and energy input for each ambient temperature bin is determined by interpolating between 5 test points.

Table 2.2: Distribution of Fractional Hours in Temperature Bins for Calculation of SEER for Central Air Conditioning Units with a 2 Speed or a Variable Speed Compressor (10 CFR, Pt 430, Subpt B, App. M, Section 6.1.2)

Bin No. j	*Bin Temperature Range (degrees Fahrenheit)*	*Representative Temperature for Bin (degrees Fahrenheit)*	*Fraction of Total Temperature Bin hours n_j/N*
1	65-69	68	.214
2	70-74	72	.231
3	75-79	77	.216
4	80-84	82	.161
5	85-89	87	.104
6	90-94	92	.052
7	95-99	97	.018
8	100-104	102	.004

Five steady-state test points are the basis of interpolating to cover the range of fixed and variable cooling capacity possibilities. A series of formulas in the variable speed part of the test procedure specify how the interpolations are performed to arrive at the appropriate value for each of the 8 temperature bins. Figure 6-1 illustrates the key aspects of the procedure graphically. A hypothetical design building cooling load is defined as 1/1.1 times the maximum speed capacity at the DOE A test condition (95^{o}F ambient, 80^{o}F/67^{o}F DB/WB indoor temperature, indicated by the square at 95^{o}F, 100%), i.e., 10% oversized. The building load is assumed to be 0 at 65^{o}F ambient temperature and is interpolated (or extrapolated) linearly at ambient temperatures above 65^{o}F. The steady-state performance of the air conditioner is tested at the five points: two outdoor temperatures at maximum speed, at two outdoor temperatures at minimum speed, and at an intermediate speed at one outdoor temperature.

- Case I (on Figure 2.29) applies to temperature bins (in Table 6-1) where the cooling capacity at minimum speed is more than the building load

- Case II applies to the temperature bins where continuous operation at an intermediate speed meets the building cooling load

- Case III applies to temperature bins where continuous operation at maximum speed does not meet the building cooling load.

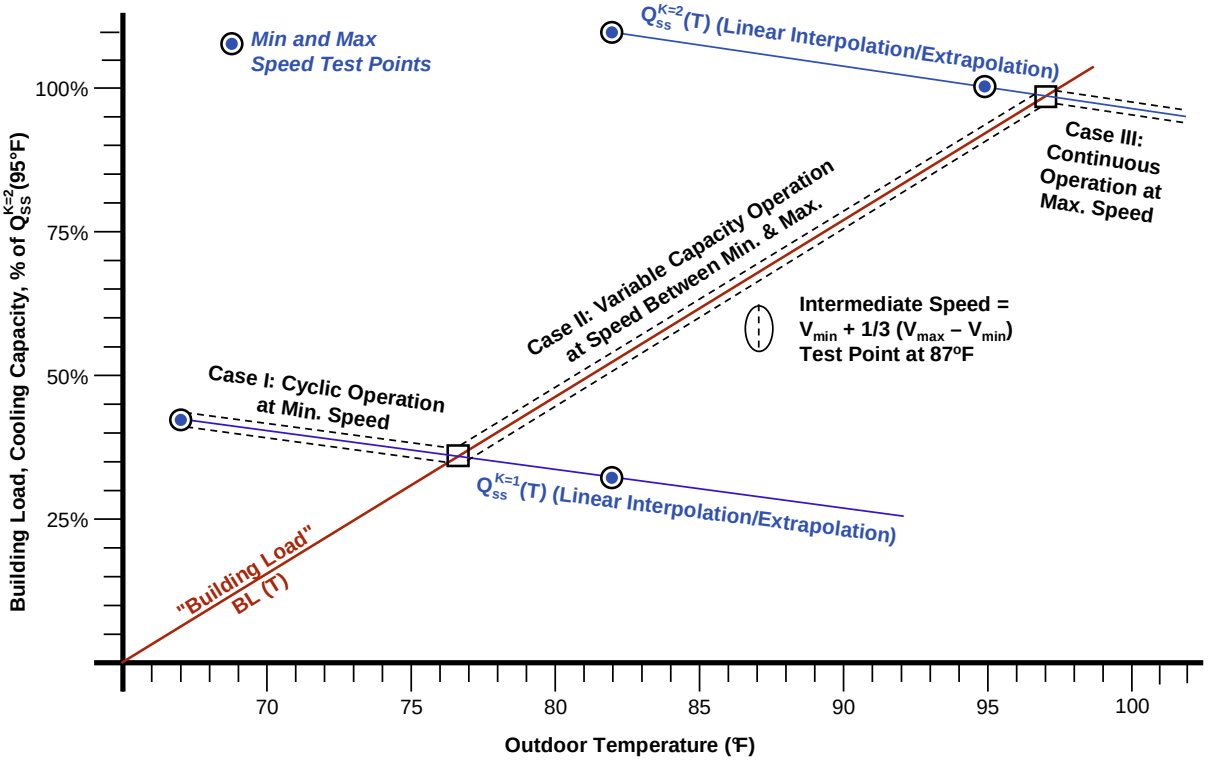

Figure 2.29: Diagram of Test Conditions for DOE Energy Efficiency Test Procedure for Variable Capacity Air Conditioner

2.8.10 Other applications and selected market data.

While the immediate focus of the project was on a 3-ton capacity residential central air conditioner, to be applied like a conventional residential split system using air ducting, the MAC technology could also be applied advantageously to other classes of conventional air conditioning equipment:

- Light commercial single package rooftop air conditioners – same seasonal efficiency advantage as residential central air conditioning split system, with the packaging advantage of short interconnecting water lines between the MAC chiller unit and the indoor and outdoor coils.
- Small air cooled or water cooled chillers – since the MAC is inherently a chiller it may be more competitive in this arena. To maintain a clean water charge within the

MAC chiller unit, it might be coupled to the warm water and chilled water loops with compact plate-frame heat exchangers.

- Ductless split systems, specifically larger capacity (8-20 tons) variable refrigerant flow (VRF) systems. In a VRF system, many individual indoor evaporator/fan units are connected to a central refrigeration unit. Because a large number of the evaporators could be inactive at any given time, a wide capacity modulation range is needed. The multiplicity of evaporators, long refrigerant lines, and wide capacity range cause oil (compressor lubricants) management problems that must be addressed in the VRF system design and add significant cost. The inherent capacity modulation and oil-free operation of the MAC could make the MAC an attractive, energy efficient, cost competitive option to VRF systems.

3 Conclusion

3.1 Rotary bed magnetic refrigerator experiments.

The rotating bed magnetic refrigerator proved to be a useful magnetocaloric material test platform. We were able to compare different materials under similar conditions, and test them over a range of flow rates, frequencies, and temperatures.

3.1.1 First order magnetocaloric materials in AMR.

Tests with $Gd_5(Si_{2.09}Ge_{1.91})_4$ in the rotary bed magnetic refrigerator showed that this particular first order phase transition magnetocaloric material suffers from hysteresis, illustrated by the decline in no-load temperature span with increasing cycle frequency. Load tests, where the heat load ranges from zero up to the maximum load show that cooling power is also reduced at increased frequency.

A good magnetic refrigerator design operates with a high specific flow rate and at a high frequency in order to generate as much cooling as possible from a given amount of magnetocaloric material and magnetized field volume. The GdSiGe material would not be a good magnetic refrigerant, because it does not perform well at high frequency.

However, we tested another first order material, LaFeSiH, under a parallel NIST ATP program. This material did not exhibit much decrease in performance with increasing frequency. The “pseudo-MCE” test results for LaFeSiH shows a fairly high peak, illustrating the large heat capacity. The peak is much sharper than any of the second order materials tested, such as gadolinium, illustrating both the need and the suitability of this material to layering in an active magnetic regenerator bed.

The fact that the Curie temperature can be tailored by controlling the hydrogen content makes it a very promising candidate for a layered bed. The Curie point of LaFeSiH can also be extended to much higher temperature than the 20 C Curie point of Gd, enhancing heat exchange capability to warm ambient conditions. The constituent materials are less costly then most other magnetocaloric materials. The challenge lies in developing the material fabrication process.

3.1.2 Layering in AMR.

Testing a bed layered with two different magnetocaloric materials clearly demonstrated the importance of layering. The bed contained half gadolinium and half gadolinium-erbium alloy. In load tests with the same hot heat sink temperature, the layered bed performed better than beds containing only one of the constituent magnetocaloric materials, producing more cooling power and a larger temperature span in the useful region between maximum cooling power and maximum temperature span.

In the "pseudo-MCE" test the layered bed exhibited a broader cooling power peak than any of the single-MCE beds, effectively working over a wide temperature range (at zero span). While the peak zero-span cooling power is lower than that for the gadolinium bed, at moderate spans the layered bed produced greater cooling power.

Layering is a promising method to produce a larger temperature span than is possible with any single material. These positive test results with second order materials illustrate that the concept of layering works, which is important because layering is critical for first order materials that only work over a narrow temperature range.

3.1.3 Future AMR beds need first order materials and layering.

The rotary bed magnetic refrigerator experiments demonstrate that first order magnetocaloric material combined with a layered bed have the potential to greatly improve the performance of a magnetic refrigerator. The successful first order material, LaFeSiH, has a large magnetocaloric effect that occurs over a small temperature range. The narrow operating range of the material means that multiple layers are required to produce a temperature span large enough for a practical refrigeration device. LaFeSiH is a promising magnetic refrigerant for a layered bed because the Curie temperature of each layer could be controlled by the amount of hydrogen added when the material is being processed.

3.2 Passive regenerator.

The losses that occur during the regeneration portion of the active magnetic regenerator cycle also occur in a passive regenerator. Passive regenerators can be fabricated from conventional materials using conventional methods. The passive regenerator test system experimentally measures regenerator ineffectiveness to compare different regenerator geometries over a range of flow rates and cycle frequencies.

3.2.1 Advanced geometry regenerators.

The goal of the passive regenerator portion of this project was to fabricate and test a number of advanced regenerator geometries in stainless steel. We planned to pick the most promising geometry for fabrication in gadolinium and use it in the SEP. For comparison, we built and tested regenerator beds packed with spherical particles and packed with irregular particles, and a bed filled with screens.

The first advanced regenerator geometry was a promising, and models led to regenerator designs with theoretically low pressure drop, low longitudinal thermal conduction, and

good solid-fluid heat transfer. Modifying this design improved performance and made it less sensitive to manufacturing tolerances, according to computational fluid dynamics analysis.

We built two passive regenerator test beds of the initial design, and after experiencing manufacturing and assembly tolerance issues, we built a bed with the modified design. Each of these enhancements improved the performance of the subsequent beds, but the geometry is still sensitive to misalignment and the results did not meet our expectations.

Instead of trying to control the critical flow channel geometry by processing the metal regenerator material, which looked even more challenging with gadolinium, we changed course and designed a bed where the flow channel would be controlled using conventional technology and materials.

3.2.2 Material and fabrication challenges.

Producing consistent, precise advanced regenerator components and then assembling them into a regular regenerator bed proved challenging. Slight manufacturing and assembly imperfections could cause uneven flow distribution in the beds. If some flow paths though a bed have lower impedance, those paths will draw more of the flow while providing less heat transfer. Other parts of the bed will experience less flow and less heat transfer.

The situation is similar for the second advanced regenerator geometry design. Slightly inconsistent geometry could cause flow maldistribution. This would cause reduced heat transfer in the bed.

We suspect that local variation in the regenerator geometry and the resulting flow mal-distribution is the main reason the advanced regenerator geometry beds did not meet expectations.

3.3 Synthesis and characterization of magnetocaloric materials.

Measurement of the properties of Gd and Gd alloys verified that the magnetocaloric properties of Gd-Er alloys changed smoothly with Er content, and the properties of Gd in another geometric form are essentially the same as that of bulk material and of spherical particles. The economics of converting Gd metal into an advanced geometry proved disappointing, presumably because of the difficulty processing Gd metal. The economics of magnetic refrigeration would clearly benefit from the use of more recent and advanced materials such as the $La(Fe_{1-x}Si_x)_{13}H_y$ series.

3.4 SEP testing.

It was challenging to find vendors who could supply sufficient quantity of gadolinium in the form we required for the SEP, so we ended up purchasing the material from two vendors. The material from one vendor was lower quality. Even the better quality gadolinium was much less consistent than the stainless steel we had been working with for passive regenerator beds.

The inconsistent quality of the gadolinium made it challenging to produce consistent components for the initial advanced geometry regenerator. The processing vendor was unable to hold the required tolerances for stainless steel, and gadolinium was even more challenging. This was one of the reasons that convinced us to pursue a regenerator geometry where the critical flow channel size was not controlled by processed metal features.

The second advanced regenerator geometry uses conventional industrial techniques to control the flow channel size. We thought using conventional technology would provide better control over the process and the resulting geometry. However, we did not achieve the desired level of regenerator component consistency. The variation geometry is main causes for suspected uneven flow distribution in the beds. Flow mal-distribution is the major reason we think the SEP performance is lower than expected. The differences in pressure drop observed among the SEP beds is evidence of the variation in geometry between the beds.

The SEP produces good cooling power, but the temperature span is disappointing. The zero-span cooling power at 3 LPM and 60 RPM is within 15% of the lossless model case. The performance is limited by higher than expected pressure drop in the beds, which limits the flow rate.

The completed SEP is a flexible magnetic refrigeration test platform. It has individual, fixed beds that can be individually instrumented, unlike rotating bed designs. The beds can also be removed or repaired separately. The SEP operates at high flow rate and frequency, allowing us to push the limits of high performance beds in the future. The high speed data acquisition system is flexible and expandable for future experiments. A unique mechanical arrangement allows measurement of the magnet drive torque and/or the valve drive torque, helping to isolate and quantify parasitic losses.

3.5 Magnetic Air Conditioning cost analysis.

TIAX developed the projected cost for 3 ton magnetic air conditioning (MAC) systems using extensive experience in technology-based manufacturing cost analysis, along with results from Astronautics models, assuming future advanced regenerators, improved materials, and estimated parasitic losses. The magnet cost was based on a detailed Astronautics design, and the MCM cost was estimated by Astronautics. TIAX estimated the heat exchanger cost using Heatcraft code, and went through multiple optimization iterations to minimize cost.

For a high efficiency MAC, the limiting factor during modeling was the EER baseline efficiency of 12.5. The resulting SEER 23 was higher than targeted, because a MAC can be optimized to operate efficiently at full power, and it will operate at higher efficiency at partial load.

Comparing the direct manufacturing cost of a high efficiency (SEER 23) MAC to a conventional high efficiency (SEER 18) vapor compression (VC) system, the MAC is 28% more efficient and 37% more costly. The cost gap closes with higher efficiency. Magnets

dominate the MAC cost. Improving the MCM, with a material with higher magnetocaloric effect than LaFeSi, would further reduce the cost.

TIAX also produced a cost stack for a lower cost version of the MAC that trades some efficiency for reduced cost. Astronautics modeled this version with a somewhat smaller magnet and reconfigured bed, while the coils remained the same. Compared to a standard efficiency (SEER 13) VC system, the standard efficiency (SEER 13) MAC is less cost competitive. The 77% decrease in SEER resulted in only 11% cost decrease.

While this analysis showed that magnetic refrigeration currently is not less expensive than conventional technology in the residential 3 ton capacity ducted air conditioning application, there are other classes of conventional air conditioning equipment where MAC could be have advantages over conventional systems. For example, magnetic refrigeration might be well suited for use as a small air cooled or water cooled chiller, since a magnetic refrigerator is inherently a chiller. MAC could also be more competitive in systems where the magnet is not such a large fraction of the total cost. In some situations magnetic refrigeration could possibly eliminate unit operations, such as a chiller where the magnetic refrigerator heat transfer fluid could be used to directly cool the load, eliminating intermediate heat exchangers. Compact and efficient plate and frame heat exchangers could be used to keep the process fluid separate from the magnetic refrigeration fluid if necessary.

4 Bibliography

C.Zimm, A.Boeder, J.Chell, A.Sternberg, A.Fujita, S.Fujieda, and K. Fukamichi, “Design and performance of a permanent-magnet rotary refrigerator”, International Journal of Refrigeration, Vol. 29, pp. 1302-6, 2006

5 List of Acronyms and Abbreviations

3TMAC	3 ton Magnetic Air Conditioner
AMR	Active Magnetic Regenerator
C	Celsius degrees
CFD	Computational Fluid Dynamics
COP	Coefficient of Performance, Watts per Watts
DSC	Digital Scanning Calorimeter
EER	Energy Efficiency Ratio
Er	Erbium
Fe	Iron
FEA	Finite Element Analysis
FOM	Figure Of Merit
Gd	Gadolinium
Ge	Germanium
GPM	Gallons Per Minute
H	Hydrogen
HVAC	Heating, Ventilation, Air Conditioning
Hz	Hertz
J	Joules
K	Kelvin
La	Lanthanum
LPM	Liters Per Minute
MAC	Magnetocaloric Air Conditioner
MCE	Magnetocaloric Effect
MCM	Magnetocaloric Material
NIST ATP	National Institutes of Standards Advanced Technology Program
PRS	Passive Regenerator System
RPM	Revolutions Per Minute
RBMR	Rotating Bed Magnetic Refrigerator
RMMR	Rotating Magnet Magnetic Refrigerator
SA	Semi-Analytical
SEER	Seasonal Energy Efficiency Ratio
SEM	Scanning Electron Microscopy
SEP	Subscale Engineering Prototype
Si	Silicon
T	Tesla
VC	Vapor Compression
W	Watt